In vivo tracking of functionally tagged Rad51 unveils a robust strategy of homology search

Siyu Liu, Judith Miné-Hattab, Marie Villemeur, Raphaël Guérois, Henrik Dahl Pinholt, Leonid Mirny, Angela Taddei

Title:

In vivo tracking of functionally tagged Rad51 unveils a robust strategy of homology search.

Author list:
Siyu Liu [1], Judith Mine-Hattab [1]‡, Marie Villemeur [1]*‡, Raphael Guerois [2], Henrik Dahl Pinholt [3], Leonid A. Mirny [1,3,4], Angela Taddei [1]*.

Affiliations:
1Institut Curie, PSL University, Sorbonne Université, CNRS, Nuclear Dynamics; Paris, France.
2Université Paris-Saclay, CEA, CNRS; Institute for Integrative Biology of the Cell (I2BC); Gif-sur-Yvette, France
3 Department of Physics, Massachusetts Institute of Technology; Cambridge, Massachusetts, USA.
4 Institute for Medical Engineering and Science, Massachusetts Institute of Technology; Cambridge, Massachusetts, USA.

* Corresponding author. Email: angela.taddei@curie.fr

Abstract

Homologous recombination (HR) is a major pathway to repair DNA double-strand breaks (DSB). HR uses an undamaged homologous DNA sequence as a template for copying the missing information, which requires identifying a homologous sequence among megabases of DNA within the crowded nucleus. In eukaryotes, the conserved Rad51-ssDNA nucleoprotein filament (NPF) performs this homology search. Although NPFs have been extensively studied in vitro by molecular and genetic approaches, their *in vivo* formation and dynamics could not thus far be assessed due to the lack of functional tagged versions of Rad51. Here, we develop and characterize in budding yeast the first fully functional, tagged version of Rad51. Following induction of a unique DSB, we observe Rad51-ssDNA forming exceedingly long filaments, spanning the whole nucleus and eventually contacting the donor sequence. Emerging filaments adopt a variety of shapes, not seen in vitro and are modulated by Rad54 and Srs2, shedding new light on the function of these factors. The filaments are also surprisingly dynamic, undergoing rounds of compaction and extension. Our biophysical models demonstrate that formation of extended filaments, and particularly their compaction-extension dynamics, constitute a robust search strategy, allowing DSB to rapidly explore the nuclear volume and thus enable efficient HR.

Main Text

Introduction

Among the different kinds of DNA insults, double-strand breaks (DSBs) are the most genotoxic. DSBs can arise from errors in DNA metabolism, such as during DNA replication, as well as by exposure to exogenous DNA-damaging agents. Failure to repair such lesions leads either to cell death or genomic instability. Homologous recombination (HR) is one of the main pathways to repair DNA DSBs and stalled replication forks [1–3]. HR uses an undamaged homologous DNA sequence as a template for copying the missing information. When available, the sister chromatid provides an ideal donor sequence as it is perfectly homologous and in spatial proximity. However, in the absence of an intact sister, homologous sequences on either the homologue or a different chromosome can be used as a template leading to inter-homologue or ectopic recombination, respectively. In this case, identifying the homologous sequence among the megabases (Mbs) of the genome within the nuclear space represents a real challenge with the risk of using the wrong donor sequence, thus leading to genomic instability [4–6].

At the molecular scale, homology sampling is carried out by a nucleoprotein filament (NPF), formed by the recombinase, RecA in bacteria and Rad51 in eukaryotes, coating ssDNA [7]. *In vitro*, this leads to a rigid right-handed helix around ssDNA, (50% extended relative to B-form duplex) [8] with a persistence length ranging from 190 to 550 nm. These micrometer-long, rigid structures could sample surrounding dsDNA in parallel, in search for a homologous sequence to use as template for repair [9].

Rad51 engages into HR following the generation of ssDNA by the combined actions of the nucleases Mre11, Exo1, and Dna2 [10]. Once generated, ssDNA is rapidly coated and stabilized by the ssDNA-binding protein complex, RPA, which is then replaced by the recombinase Rad51 [2]. While Rad51 filament formation is a key step for HR, it is also potentially harmful for cells if intermediates are formed that cannot be processed normally [11]. Several regulators of Rad51 filament formation and stability have been identified including the recombinase loader Rad52, the helicase Srs2, and the member of the SNF2 family of chromatin remodeling DNA-dependent ATPase Rad54 [9,12].

Although Rad51 has been extensively studied through genetics, *in vitro* analyses, structural and molecular approaches [2,7,9,12,13], how the nucleofilament is being formed, and how it mediates homology search *in vivo* remained elusive, owing to the lack of functional tag to monitor Rad51 in living cells. While micrometer long RecA structures are observed upon DSB in bacteria [14,15], cells expressing terminal tagged version of Rad51 showed unresolved foci at DSB sites in

eukaryotic cells [16–18], in contradiction with the long rigid structures predicted from *in vitro* studies.

Here we established the first functional tagged version of the eukaryotic recombinase Rad51, thanks to which, we could follow the dynamics of Rad51 assemblies undertaking homology search in living cells.

Results

A functional tagged version of Rad51

So far, no version of fluorescent tagged Rad51 has been shown to be fully functional. We reasoned that the difficulty to design a functional Rad51 tag was due to the structural constraints imposed to form a functional filament and allow access to regulatory factors. Taking in consideration these physical constraints, we thought to introduce a fluorescent tag in the least conserved region of the N-terminal domain of Rad51 of *Saccharomyces cerevisiae* (Fig. 1A). After several adjustments of GFP version and linker properties, we obtained an endogenous tagged version of Rad51 (Rad51-iGFP2, Fig1B ; here after Rad51-iGFP), which allowed wild-type resistance to the damaging agent MMS when expressed as the only copy of *RAD51*, in contrast to the commonly used N or C-terminal tagged versions (Fig. 1B [16,17]).

Furthermore, our tagged version of Rad51 is as competent as the wild-type version to perform gene conversion following the induction of a unique DSB in the presence of a homologous donor sequence located on a different chromosome (Fig. 1C).

Finally, we checked by western blot that the GFP tag did not affect the expression levels of Rad51 even following the induction of an irrepairable DSB by the I-*Sce*I endonuclease (Extended Fig. 1A).

Together, these data show that our internally tagged version of Rad51 is functional for homologous recombination. We could thus use this system to monitor Rad51 during HR events.

Rad51 forms filaments to perform homology search *in vivo*

Using our functional Rad51-iGFP expressing strain, we monitored Rad51 localization *in vivo* before and after induction of a unique irrepairable DSB in haploid cells. In the absence of induced DSB, we observed spontaneous foci in 5 % of the cells (Fig. 1D) as previously shown using a N-terminal tagged version of Rad51 [16]. Similar foci are visible in cells 2 hours after I-*Sce*I induction, together with brighter globular and elongated structures that were not reported for strains expressing either N- or C-terminal tagged Rad51 (Extended Fig. 1B-C [16,17]).

The percentage of cells showing Rad51 structures, quantified using machine-learning-based image analysis [19], increased over time after induction reaching 90 % after 6 hours (Fig. 1D-E and Extended Fig. 2A). The proportion of elongated structures as well as their length also increased over time, some of them exceeding 1 µm in length at late time points (see below for quantification) akin the RecA filaments observed in bacteria [14,15]. Here, we use the term filaments to refer to Rad51 elongated structures and NPFs to refer to the nucleoproteic filaments.

We observed similar filaments by immuno-fluorescence in untagged cells using an antibody raised against Rad51, after inducing an un-repairable DSB (Fig. 1F), ruling out potential artefact owing to the presence of the tag.

Filamentous structures were also observed in diploid cells, in which the homologous chromosome provide a perfect donor sequence, as well as in haploid cells that carry a donor sequence located on the same chromosome (Extended Fig. 2B-C, Extended Fig. 3A-B). However, the proportion of cells showing Rad51 filaments is reduced in the presence of a donor sequence 4 hours after DSB induction, reflecting the repair of the DSB (see below). In contrast, Rad51-iGFP forms mainly foci upon release from replication stress (Extended Fig. 4A), suggesting that Rad51 filaments are associated with the process of homology search. In all situations, Rad51 structures were observed mainly in S and G2/M phases, as expected (Extended Fig. 4B-C).

In a diploid strain, the percentage of cells showing Rad51 structures peaks 4 hours after induction, a timing consistent with the disassembly of the nucleofilament once HR is achieved (Fig. 1G). We next assessed which of the Rad51 structures interact with the donor sequence on the homologous chromosome, tagged with the FROS system (Fig. 1H). Rad51 filaments showed a maximal level of association (50%) 2 hours after DSB induction, in good agreement with the kinetic of homologous pairing observed in living cells [20] and ectopic donor invasion monitored by molecular assay [21–23]. In contrast, Rad51 foci or globular structures associate 3-fold less with the donor sequence, showing little variation over time after DSB induction, and a rate close to the one observed for association with a non-homologous FROS tagged sequence (Fig. 1H middle panel). These results suggest that Rad51 filaments observed here in living cells correspond to the functional structures involved in homology search and strand invasion.

Rad51 filament formation requires Rad52 and long ssDNA

We next tested in living cells, the impact of factors identified as Rad51 regulators through genetic and molecular studies. We first verified that the formation of Rad51 filaments and foci

requires the Rad51 loader Rad52. Consistently, Rad51 nuclear structures were rarely observed in *rad52*Δ cells (less than 1%) 4 hours after DSB induction (Fig. 2A). To test whether Rad51 filament form on single strand DNA we deleted either *EXO1* or *SGS1*, which both contribute to the long range resection of DSB [10]. Both deletions decreased the number of cells showing Rad51 filament 4 hours after DSB induction (Fig. 2A-B). Moreover, the double *sgs1*Δ *exo1*Δ strain, where long-range resection is abolished, shows very few Rad51 structures with weaker intensity than the wildtype strain 4 hours after DSB induction (Fig. 2A-B and Extended Fig. 5A). We thus conclude that the extension of Rad51 filaments requires long-range resection.

After deconvolution and segmentation, we measured the distribution of Rad51 filaments length over 2, 4 and 6 h DSB induction in haploid and diploid strains (Fig. 2C and Extended Fig. 5B). We observed a broad distribution of filament lengths which median increased over time, in haploid cells in the absence of a donor sequence (MED ± SDV: 0.9 ± 0.8 µm at 2h, 1.3 ± 0.9 µm at 4h and 1.7 ±1.1 µm at 6h after DSB induction; 214, 373 and 268 filaments analyzed respectively). Diploid cells show longer filaments at 2h and 4h (respectively 1.3 ± 0.9 and 1.7 ±1µm, 180 and 359 filaments analyzed), reflecting the higher efficiency of the HR pathway in diploid versus haploid cells. In contrast, filaments are shorter after 6 hours in diploid cells (1.4 ± 0.9 µm), where the DSB can be repaired using the homologous chromosome as a perfect donor sequence.

In vitro, Rad51 coated ssDNA is extended by 50% relative to B-form duplex [8]. Assuming a similar extension *in vivo*, 1 µm would correspond to approximately 2 kb of ssDNA. This is consistent with chromatin immunoprecipitation (ChIP) performed against Rad51, 4 hours after I-*Sce*I induction showing a broad 4-6Kb peak for both tagged and untagged versions of Rad51 (Fig. 2D). Therefore, the length of the Rad51 filaments that we observe *in vivo* is compatible with the extent of DSB resection and Rad51 association as detected by ChIP.

Rad51 filaments are modulated by Srs2 and Rad54

To avoid the generation of toxic filaments and protect favorable ones, many regulators participate in the competition between dismantling and stabilizing NPF [9,12]. The Srs2 helicase is proposed to be the major negative modulator that restricts HR by disassembling the NPF. Rad54 is a critical HR factor, with both pre-synaptic and post-synaptic functions, as it was shown to stabilize the presynaptic complex, destabilize dsDNA-bound Rad51, promote strand invasion, catalyze branch migration, remodel nucleosomes, and promote strand invasion on chromatin substrates[13]. We observed Rad51 filaments in both *rad54Δ* and *srs2Δ* strains in the

absence of DSB (Fig. 3A-B), suggesting that both Srs2 and Rad54 prevent the formation of filaments at spontaneous damage. Following DSB induction, these two mutants showed more Rad51 structures after 2 hours, but similar levels after 4h.

However, our quantification revealed that the filaments are also getting longer in the *rad54Δ* (p=1E-4) strain than those in the WT strain. Although the ability of Rad54 to remove Rad51 from dsDNA was mainly proposed to act on the heteroduplex dsDNA product of strand invasion, our results indicate a presynaptic role of Rad54, possibly preventing the formation of rad51 filaments on the dsDNA flanking the damaged site. Further supporting this hypothesis, deleting *RAD54* in strains defective for long-range resection also led to the formation of longer and brighter Rad51 structures 4 hours after I-*Sce*I induction (Extended Fig. 6A-B).

In the absence of the helicase Srs2, Rad51 filament median length was not significantly affected, although we observe a decrease in the proportion of short filaments. Furthermore, Rad51 filaments are brighter in the *srs2*Δ strain (p=6E-14), which could be interpreted as an increased density of Rad51 along the filament, probably related to the known activity of Srs2 that dismantles Rad51 on ssDNA *in vitro* [12]. We thus conclude that the formation of Rad51 filaments in living cells requires the Rad51 loader Rad52, and is negatively regulated by the Srs2 helicase and the ATPase Rad54, in good agreement with activities reported for these factors [9,12].

Recurrent patterns in Rad51 filaments are regulated by Rad54

We noticed that Rad51 filaments can adopt a variety of patterns (Fig. 3D and Extended Fig. Fig. 7A-B) that we categorized into 5 subclasses: rods, bent filaments, circles, branched structures with a single node and others (including more complex or multiple structures). All these structures were also observed by immunofluorescence against the endogenous untagged Rad51 protein (Extended Fig. 7C). Rad51 mainly forms rods and bent filaments at an early stage after DSB induction, while other shapes are observed generally after a 6 hours galactose induction in the wild-type strain, suggesting that the simple filaments convert into branched and circular structures over time (Fig. 3E and Extended Fig. 7A). The same classes of structures were observed in the diploid strain, where the DSB is repaired, with a significantly lower proportion of very complex structures after 6 hours ("others" in Fig 3D and Extended Fig. 7B; p= 2E-4). We thus conclude that rod filaments, bent filaments, 1-node and circles filaments are all functional structures.

Quantifying these subclasses on strains with different genetic backgrounds, we observed that *srs2*Δ strain show a close to wildtype distribution (Fig. 3E and Extended Fig. 8A). However,

we noticed that rods and bent filaments are significantly longer in this strain (Extended Fig. 8B) in good agreement with the anti-recombinase activity of Srs2[12]. Strikingly, *rad54Δ* strain has nearly no branched filaments but accumulates circular structures (>25% at 6 hours after DSB induction versus less than 10%, in WT and *srs2Δ,* Fig. 3E and Extended Fig. 8A).

Although we expect up to four NPF in each cell (corresponding to the two sides of the break on the two sister chromatids), most cells show a single Rad51 structure. These structures thus correspond to up to four NPFs, which precise organization need to be determined. The one-node structures showing a maximum of 4 branches and being Rad54 dependent could correspond to individual NPFs interacting with small tracks of homology belonging to different parts of the genome[13]. Although there is no homologous sequence available for a faithful HR event in this case, short tracks of homology (9 to 15 nt) are sufficient for Rad54 to promote association of the presynaptic complex with dsDNA *in vitro* [24].

Together this analysis shows that timing and shapes of nuclear-size structures formed by Rad51 filaments are controlled by Srs2 and Rad54, possibly through modulation of Rad51 polymerization and depolymerization, and capacity to invade dsDNA.

Rad51 filaments undergo cycles of compaction and extension

To monitor the dynamics of Rad51 filament formation in living cells, we acquired time-lapse images, taking one Z-stack of 21 images every 5 min, starting 90 min after I-*Sce*I induction. As shown in Fig. 4A, Rad51 first accumulates as a focus, whose intensity increases, before forming a more elongated structure or filament (Movie S1). Imaging cells at 2 min time intervals (Extended Fig. 9A) we could estimate the median time between the appearance of the first focus and the formation of a structure larger than 300 nm as 22 min in wild-type cells (n=12). Consistently, this transition was faster in the absence of Srs2 or Rad54 (9 and 8.23 min respectively, Extended Fig. 9B), indicating that both factors delay Rad51 filament elongation.

Once formed, Rad51 filaments are very dynamic, bending, changing orientation and shapes over time, switching from rod to bent filaments, to more complex structures, eventually disappearing in diploid cells, probably as a result of repair events (Fig. 4B, Movie S2-4-5; and Extended Fig. 9C-D). All classes of filament shapes observed in a population of cells could be observed in single movies. Therefore, the different classes of filament shapes reflect the dynamics behavior of Rad51 structures, rather than cell to cell variability. Furthermore, we frequently observed abrupt changes in filament length, seemingly collapsing as bright foci, yet followed by a rapid re-extension (Fig. 4C and Extended Fig. 9C, Movies S3-4). Careful inspection of individual Z-stack confirmed that these foci did not correspond to filaments

truncated in the Z axis or oriented perpendicularly to the XY plane. Furthermore, the intensity of these foci was close to the total intensity of the extended filaments observed on the previous and following frames (Fig. 4D, grey, green, and purple areas for examples). We thus conclude that these bright foci are compacted filaments. This is reminiscent to the contraction events observed *in vitro* on Rad51 nucleoprotein filaments, which are hydrolyzing ATP, leading to shorter filaments associated with Rad51-ADP molecules that dissociate slowly from DNA [25,26]. In contrast with *in vitro* studies performed on dsDNA, the Rad51-K191R mutant that can bind but poorly hydrolyse ATP [27] is defective in forming long filaments in living cells (Extended Fig. 10A), preventing us from testing the impact of ATP hydrolysis on filament compaction.

Within over 26 hours of movies imaged at a 2 min rate we observed on average one contraction event every 18 min, lasting less than 5 min (1 or 2 frames). These events also occur in the absence of Srs2 or Rad54 (Extended Fig. 10B-C, Movies S6-7) indicating that none of these factors are necessary for these events.

After each compaction event the filament can extend in a different direction, thus exploring a new fraction of the nuclear volume. The range of direction covered during 80 min, as illustrated by the superimposition of filament direction acquired every 2 min, suggests that these dynamics could be a very efficient strategy for homology search.

Rad51 filaments dynamics allow a fast and robust search

Finding the homologous (donor) sequence among megabases of DNA is a rate-limiting step for HR [28,29]. Inter-homologue recombination, however, is highly efficient in diploid cells, despite a large initial separation (~1.5 μm [20]) between the DSB and the homologous locus, and highly constrained (Rouse) chromosome dynamics due to its polymer nature [30].

Whereas previous homology search models assumed that the DSB and donor locus performed random walks in space (i.e., normal Brownian diffusion)[31], here we model the chromatin loci as undergoing Rouse diffusion, consistent with the polymer nature of chromosomes and more recent experimental measurements [32,33]. To understand whether the observed compaction-extension dynamics dynamics of the filament can facilitate the search, we developed a biophysical model of the process. We considered various scenarios of search (Fig. 5A): (i) “no filament” where the DSB and the donor are compact chromosomal loci undergoing polymer dynamics; (ii) the “static filament” where the DSB proximal region is stretched into a stable filament, while the donor searches via polymer dynamics; (iii) the “dynamic filament”, where the filament undergoes rounds of extension and compaction.

We used three approaches to model the search process: First, we developed a simple model based on the properties of the Rouse diffusion to estimate search times for three scenarios and gain an intuition for how the filament can accelerate search. Second, we simulated Rouse search trajectories, validating the theory and obtaining the full distribution of the search times. Third, we developed a full polymer model of the yeast nucleus (following [34], see SI) and explicitly simulated dynamics of chromosomes and of the filament.

In all models a compact donor starts at a random position and explores the nuclear volume in search for the DSB-proximal region (compact or filamentous); the search ends when the donor touches the DSB-proximal region. As mentioned above, chromosomal loci undergo Rouse diffusion ($MSD = At^{0.5}$) that is well-supported by a broad range of locus-tracking experiments [32,33]. Rouse diffusion leads to search via compact exploration of the volume, and allows estimating the search time as the time it takes the Rouse-diffusing donor to explore the nuclear volume (see [35], and SI).

Consistently all our models demonstrated that the search without the filament is exceedingly slow (median 6-9h), while formation of the filament can considerably speed-up the search with most of the cells completing it by 2h (Fig 5C,E).

This acceleration for the static filament is achieved because irrespective of where the donor touches the filament it can recognize the complementarity -- the compact donor contains a region complementary to any part of the filament (the Brouwer fixed point theorem). The filament gives a considerable advantage because it can be reached from a much larger volume, and hence found much faster (Fig 5B,C).

Dynamically compacting and extending filament (scenario III) makes the search process even more efficient, by probing different parts of the nuclear volume on each round of extension (Fig 5B). In each round, a new section of the nuclear volume is probed by the extended filament for time $\boldsymbol{\tau}$, followed by the compacted state for time $\boldsymbol{\tau_0}$. We demonstrated (see SI) that this process is similar to other intermittent search processes[36], from animal foraging to 1D/3D protein-DNA search, where rounds of local exploration (e.g., sliding in 1D or an extended filament) are combined with flights (3D diffusion or re-extension). Like in other intermittent search processes, there is an optimal time for having a stable filament: having filament for a shorter period of time would require more rounds of search each incurring additional time in the less-exposed compacted state, while having a filament stable for too long makes the whole process inefficient due to redundant probing of the same part of the nuclear volume. Consistently, both

theory and simulations show (Fig. 5D) that experimentally measured $\tau \approx 1000$sec, provide very fast search, that is close yet slower than the optimal.

Our estimates have several functional consequences. Cells need to complete search within 8-10h, before cells adapt to checkpoint activation and undergo cell division despite the presence of an unrepaired broken chromosome [37,38], such strategy has an important evolutionary advantage [39]. Cumulative distributions of the search time (Fig 5C-E) show that considered scenarios differ in their ability to provide robust search by 8-10h. While the no-filament case is exceedingly slow (median >6-9h) and inefficient (~50% completion by 8h), and the dynamic filament is fast (median 1-2h) and robust (90-100% completion), the static filament shows an interesting fast yet not so robust search. While trajectories that originate close to the static filament finish fast, others take a long time to explore the volume until they reach the filament, as evident from the jump of the cumulative distribution for small times (Fig 5C). In polymer simulations, where the stable filament moves in space and thus sweeps a larger volume, such a fraction of fast trajectories is larger (Fig 5E). This suggests that the high mobility of the filament that we observe in microscopy during each round of extension (Fig 4) can further facilitate the search process.

Beyond considered mechanisms, the search can be further limited by the time ssDNA/Rad51 takes to interrogate dsDNA regions for homology and by the progressive loss of the homologous sequence owing from exonuclease activities, in the case of ectopic recombination[29]. Together, our biophysical modeling demonstrates that formation of elongated filaments and particularly their rapid compaction and re-extension provides a fast and robust search strategy, like other intermittent search strategies.

Discussion

Here we report the first functional tagged version of a eukaryotic recombinase allowing to monitor the dynamics of the nucleofilament upon homology search in living cells. We inserted the GFP tag in the least conserved part of the disordered N-terminal tail, *i.e.* where the insertions/deletions were most tolerated through evolution. Although the disordered N-terminus of other Rad51 orthologs or paralogs is often shorter than that of *S. cerevisiae*, it is plausible that the same strategy would also work to tag these recombinases. Our study suggests that the nucleus-wide homology search proceeds through a mechanism that is radically different from a commonly accepted view where the DSB seeks the donor as a compact focus through passive polymer diffusion. In contrast, we show that homology search is performed by micrometer long Rad51 filaments, exposing the ssDNA to a big area of the nucleus and allowing the

simultaneous scanning of sequences located in different nuclear region in good agreement with observed complex genomic rearrangement [6]. Furthermore, our study reveals that Rad51 filaments are dynamic, occasionally compacting and extending; Such dynamics facilitates the search allowing robust exploration of the nuclear volume, despite localized (Rouse) chromosome dynamics, achieving search time compatible with the repair efficiencies observed *in vivo*. Consistently, we observe a strong correlation between the ability of the different Rad51 tagged version to form long filaments and HR efficiency. While Rad51 filament dynamics ensures that the resected ssDNA can reach the donor sequence, other factors such as decreased nucleosome occupancy could facilitate the invasion of the template sequence once in proximity [40]. The observations of active dynamics of the Rad51 filament reported here suggests possible reinterpretation of previous work. For instance, the active extension of the filament itself could be in fact the cause of the increased in mobility reported for the damaged chromatin and to a lesser extent the undamaged chromatin upon DSB induction [20,41]. Finally, the capacity to monitor the dynamics of Rad51 in living cells opens new avenues to screen genetic factors and small molecules impacting on HR regulation with strong implications for both our understanding of HR regulation in living cells and the development of new intervention of therapeutic value.

Acknowledgments:

The authors thank Michael Lisby (University of Copenhagen, Danmark); and Loraine Symington (Columbia Universtity, NY, USA) for sharing strains, Mickael Garnier for his help on image analysis, Alexandre Dubos-Taddei for his help in exploring movies, the members of the Taddei and Mirny laboratories, Aurèle Piazza and Eric Coïc for helpful discussions, Bruce Futcher and Valérie Borde for sharing reagents, Geneviève Almouzni for her critical reading of the manuscript. A.T. team was financially supported by funding from the Labex DEEP (ANR-11-LABEX-0044 DEEP and ANR-10-IDEX-0001-02 PSL), PIC3I IC-CEA 2020 and CNRS grant 80prime PhONeS. Siyu Liu received funding from the CNRS MITI, LM is supported by Chaire d'excellence internationale Blaise Pascal by the Île-de-France region. The authors greatly acknowledge the PICT-IBiSA@Pasteur Imaging Facility of the Institut Curie, member of the France Bioimaging National Infrastructure (ANR-10-INBS-04).

Author contributions statement:

S.L. and M.V. generated strains and performed experiments. S.L. and J.M.H. quantified microscopy experiments. R.G. designed the Rad51 tagging strategy. L.M. performed the modeling and supervised H.D.P who performed polymer simulations A.T., S.L., M.V. and J.M.H. contributed to the design of the experiments. All contributed to the interpretation of the data, the drafting of the figures, and the writing/revision of the manuscript.

Competing interests Statement: An invention disclosure related to the results was submitted to Insitut Curie Technology Transfer Office for filing a patent application.

Figure Legends:

Fig. 1: Rad51 forms filaments upon DSB to perform homology search in living cells

A. Strategy to tag Rad51. Top: a single monomer of RAD51-iGFP2 with positions of Rad51 amino acids shown as spheres colored with respect to their conservation in Rad51 homologs. It highlights that the N-terminal tail of RAD51contains sequence motifs partially conserved among closely related yeasts to *S. cerevisiae.* The GFP was inserted just downstream of these motifs in the least conserved stretch of amino acids. Bottom: the structure of the nucleofilament formed by Rad51-iGFP2 around ssDNA.

B. Sensitivity of WT, *rad51*Δ, N-terminally tagged YFP-Rad51, and our internally tagged Rad51-iGFP expressing strains to the genotoxic agent Methyl Methane Sulfonate (MMS). **C.** Schematic description of the galactose induced DSB by I-*Sce*I and average survival rate of the untagged or Rad51-iGFP strain upon DSB induction (n=2442 colonies in 4 experiments) in the presence or absence of a donor sequence. **D.** Representative images (Transmitted-light image and the GFP fluorescent image) of a Rad51-iGFP expressing strain at different time after DSB induction. Z-projection is applied on fluorescent images. Min and max intensity fluorescence intensities are indicated. **E.** Average percentages of Rad51 foci, globular structures, and filaments at different time after DSB induction (n=2108 cells examined over 2 experiments). **F.** Untagged Rad51 localized by Immunofluorescence 4 hours after DSB induction. **G.** Average percentages of Rad51 structures in haploid (without donor) and diploid strains over time after DSB induction (n=7114 cells over 3 experiments). **H.** Top: Schematic representation of the strains used to monitor the donor locus (on the homologous chromosome) or a control locus (on another chromosome, to account for the random encounter of Rad51 structures with the locus), labelled by insertion of lacO array in a strain expressing RFP-LacI and Rad51-iGFP strain. Bottom: average percentages of Rad51 foci/globular structures or filaments associated with lacO array at different time after DSB induction (examples of lacO spot associated or not associated with Rad51 are shown on the right). n=687 Rad51 structures over 2 experiments.

Scale bars: 2µm. Data are presented as mean values +/- SEM.

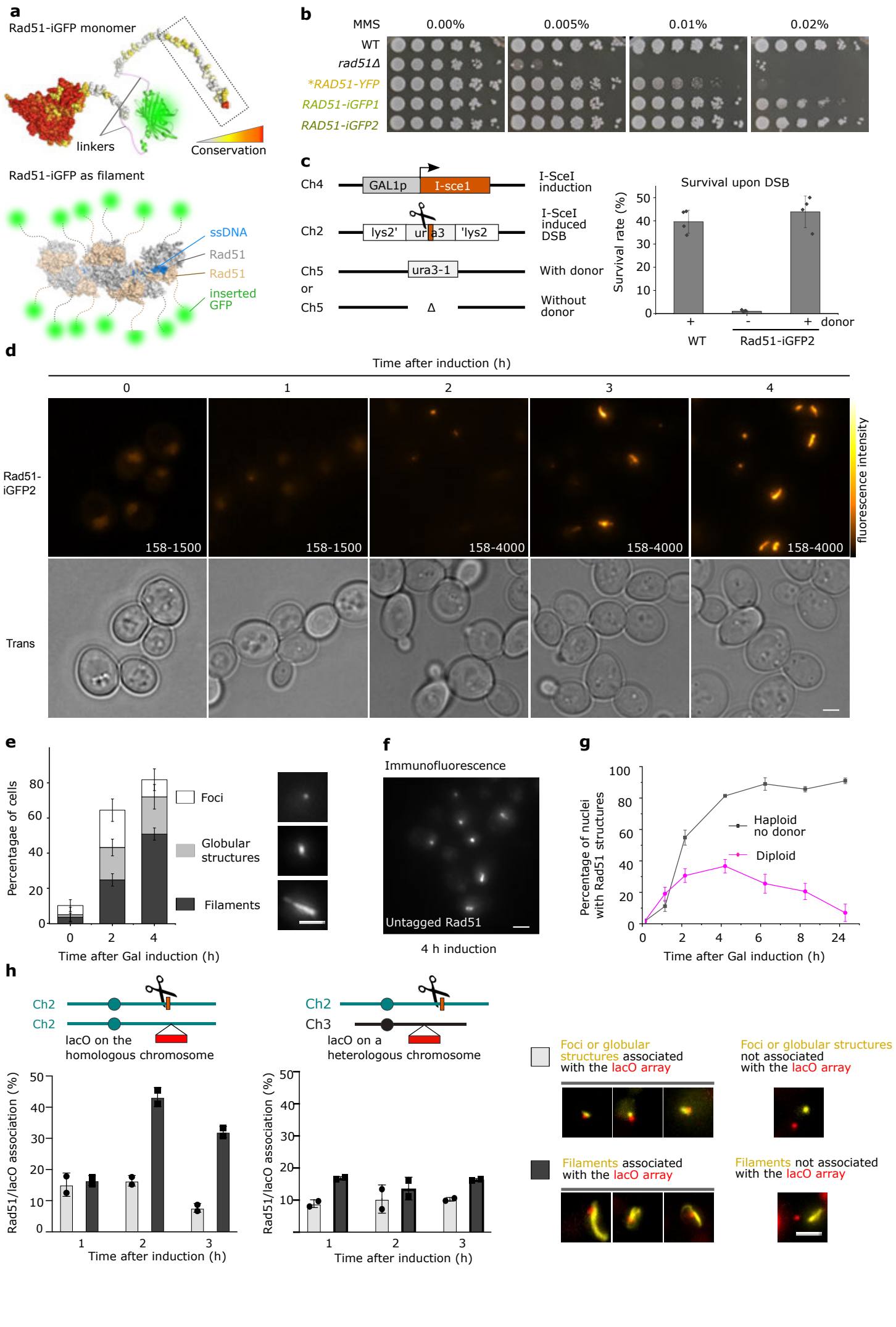

Liu et al., Figure 1

Fig. 2. Rad51 forms micrometer long filaments on ssDNA

A. Z projection of GFP images in WT*, rad52*Δ*, exo1⊿, sgs1⊿,* and *exo1sgs1* strains expressing Rad51-iGFP 4h after DSB induction. **B.** Average percentages of Rad51 foci, globular structures and filaments in WT and mutant strains. Data obtained through ilastik [19], n=4432 cells in 2 experiments. Statistical significance on the percentage of Rad51 filaments is calculated through Prism(two-sided Fisher's exact test,**** represents p value<0.0001, p=0.6489 for 2h WT vs *exo1⊿,*, p=0.2832 for 2h WT vs *sgs1⊿*) **C.** Distribution of filaments 3D lengths after 2, 4 and 6 h of galactose induction in haploid (un-repairable DSB) and diploid strains (where the homologous chromosome provides a donor sequence for HR), n=1720 filaments analyzed from 2 independent experiments. **D.** Average enrichment of Rad51 as a function of the distance from the DSB site monitored by ChIP on *RAD51, RAD51-iGFP1, RAD51-iGFP2* and *rad51⊿* strains, 4 hours after DSB induction (n=24 biologically independent samples examined over 3 experiments), * represents positions of primers used in ChIP.

Error bars: standard errors.

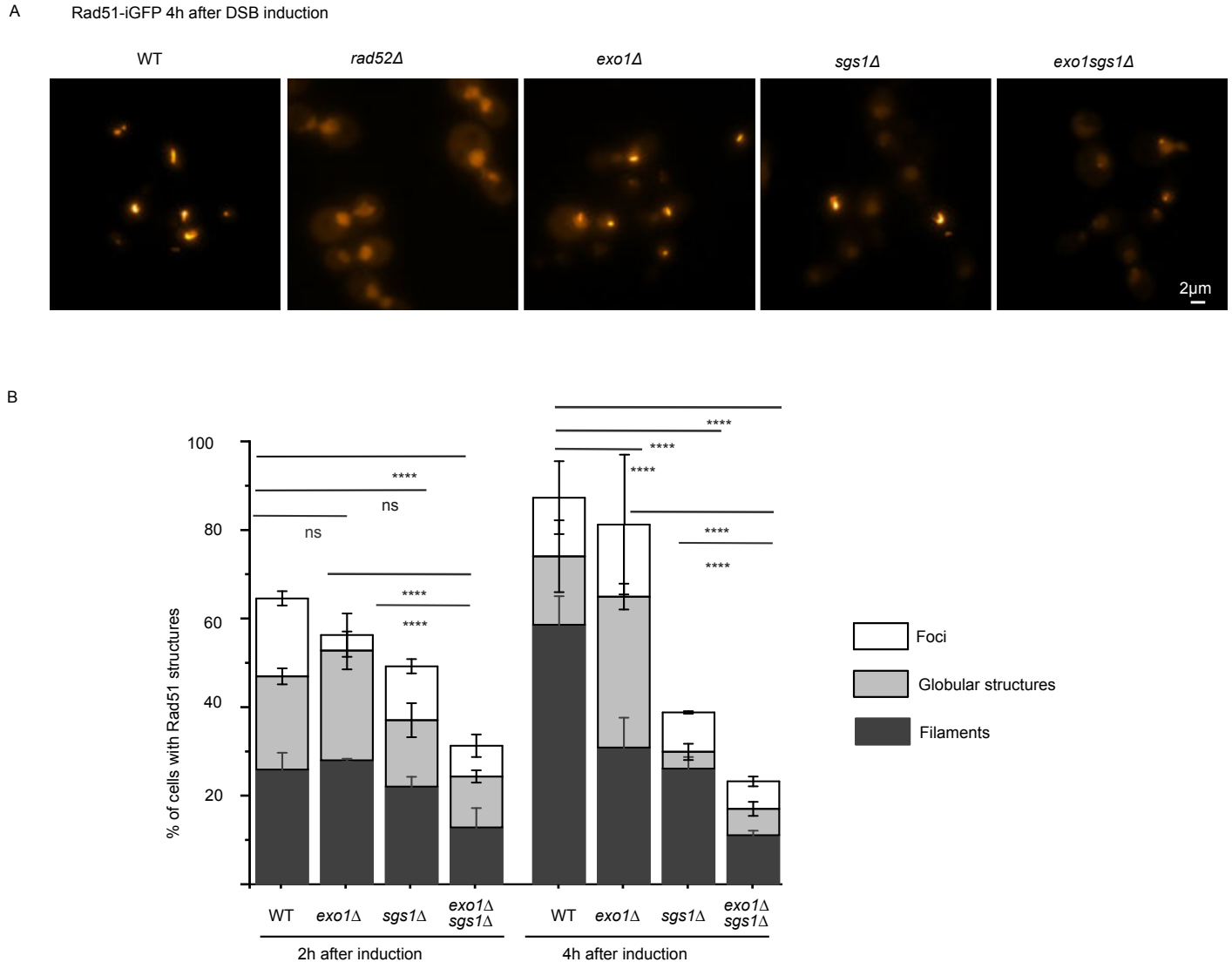
A
Rad51-iGFP 4h after DSB induction
WT
rad52Δ
exo1Δ
sgs1Δ
exo1sgs1Δ
2µm
B
% of cells with Rad51 structures
100
80
60
40
20
ns
ns
****
****
****
****
****
****
****
****
WT
exo1Δ
sgs1Δ
exo1Δ sgs1Δ
WT
exo1Δ
sgs1Δ
exo1Δ sgs1Δ
2h after induction
4h after induction
Foci
Globular structures
Filaments
C
Deconvolution
Segmentation
1µm
Haploids
Diploids
mean
median
Filaments length (µm)
7
6
5
4
3
2
1
2 h
4 h
6 h
2 h
4 h
6 h
Time of DSB induction
D
ChIP against Rad51
4h after gal induction
Enrichment over OGG1 normalized by rad51Δ
40
30
20
10
0
RAD51
RAD51-iGFP V1
RAD51-iGFP V2
rad51Δ
0
2
4
6
8
10
12
14
16
18
20
Distance from I-sceI cut site (kb)
lys2

Fig. 3. Rad51 filament structures are regulated by Rad52, Srs2 and Rad54.

A. Representative images of RAD51-iGFP 4h after galactose induction in WT, *srs2⊿*, and *rad54⊿* strains. **B.** Average percentages of Rad51 foci, globular structures, and filaments in the indicated strains. Data obtained through Ilastik [19], n=6464 cells in 3 experiments. Statistical significance on the percentage of Rad51 filaments is calculated by two-sided Fisher's exact test using Prism (**** represents p <0.001,* for p<0.05, ns for p>0.05; 2h WT vs *srs2⊿* p>0.9999, WT vs *rad54⊿* p=0.3445; 4h WT vs *srs2⊿* p=0.0354, WT vs *rad54⊿* p=0.0853). **C.** Comparison of mean intensities within Rad51 filaments and their lengths in WT and mutant strains (n=519 filaments are analyzed). On each box, the central mark indicates the median, and the bottom and top edges of the box indicate the 25th and 75th percentiles, respectively. The whiskers extend to the most extreme data points not considered outliers, and the outliers are plotted individually using the '+' marker symbol. Statistical test: Two-sided Wilcoxon rank sum test (*** represents p<0.001,** p<0.01,* p<0.05; Intensity, WT vs *srs2⊿* p<0.0001, WT vs *rad54⊿* p=0.0056; Length WT vs *srs2⊿* p=0.1, WT vs *rad54⊿* p=0.0004). **D.** 5 classes of Rad51 filaments are observed. **E.** Distribution of the 5 classes in WT (haploid and diploid), *srs2⊿, and rad54⊿* strains after 2, 4, 6h DSB induction, and presentative filaments 4 h after induction. Scale bars: 2μm.

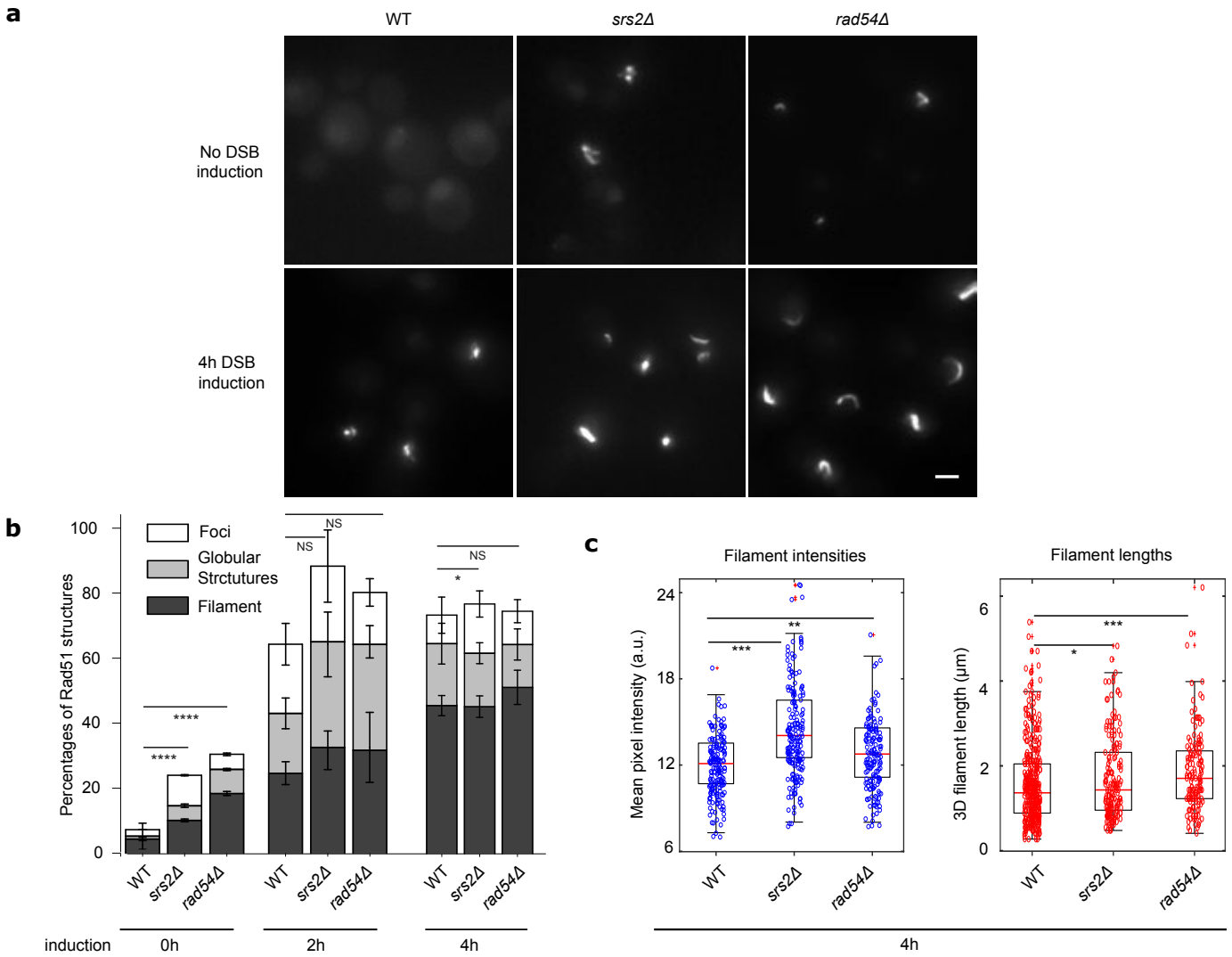

Liu et al., Figure 3

Fig. 4. *In vivo* dynamics of Rad51 filaments.

A-B. Representative time-lapse images acquired every 5 min, 90 min after galactose addition (I-SceI induction) showing the formation of Rad 51 filament (A, Movie S1), or 150 min after Galactose addition (B, Movie S2) showing the dynamic of a mature Rad51 filament adopting different shapes over time. **C.** Images acquired every 2 mins, 70 min after galactose addition showing Rad51 filament undergoing compaction and extension events (Movie S3). **D.** Normalized fluorescence intensity and 3D length over time of the images shown in C. **E.** Superimposition of the direction of filaments shown in C. Scale bars: 2 μm.

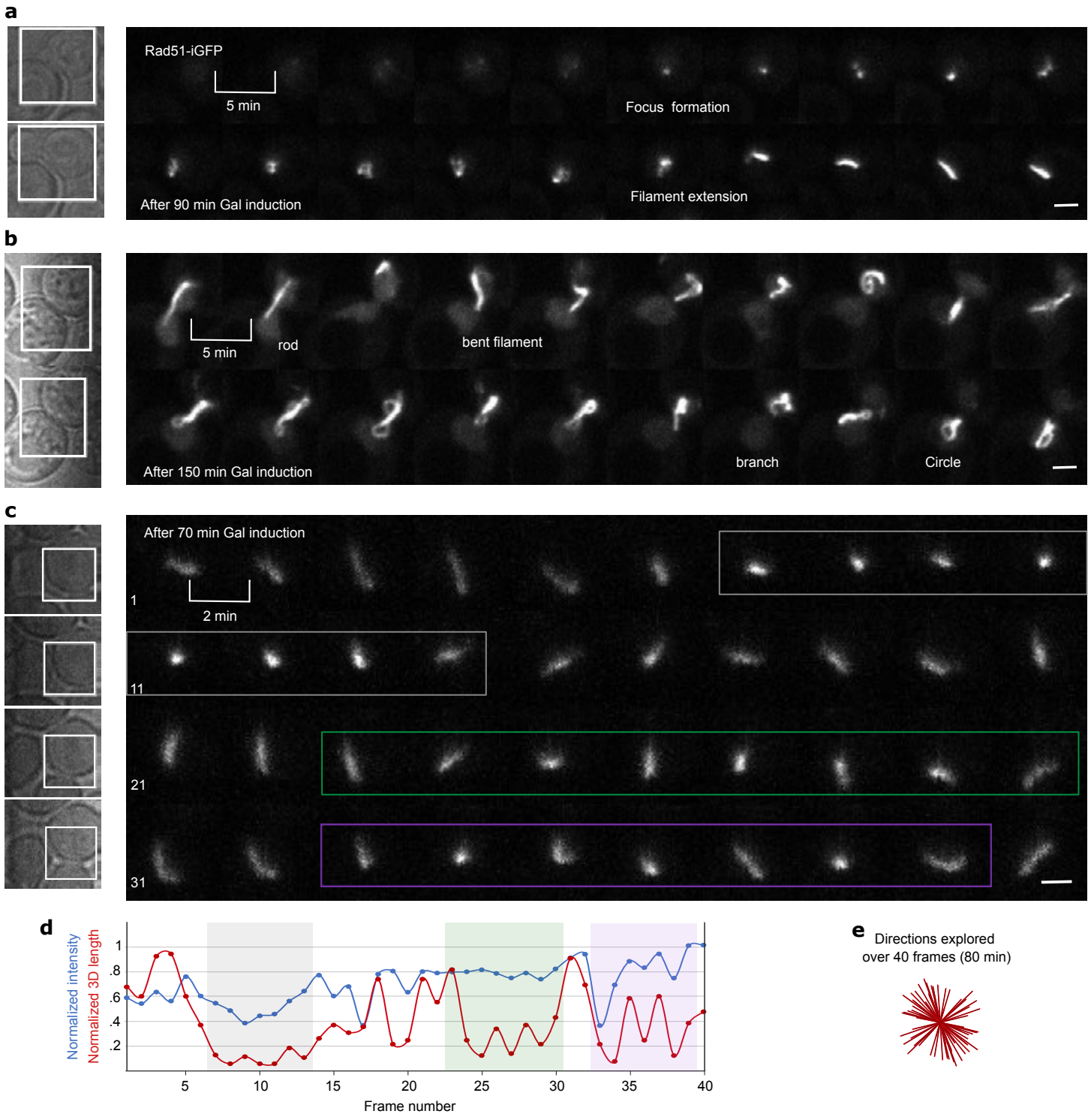

Liu et al., Figure 4

Fig 5. Fast and robust search is facilitated by Rad 51 filament dynamics.

A. Different scenarios for homology search. Scenario I: the nuclear space is explored by two loci (the DSB and the donor) each undergoing Rouse diffusion (with D=.01 $\mu m^2.s^{-1/2}$); Scenario II: a static filament (of length 1.2 μm), and a locus of the donor undergoing Rouse diffusion. Scenario III, a dynamic filament undergoing cycles of extension and compaction, while the locus of the donor is performing Rouse diffusion. The yellow areas illustrate the volume explored over time. Art by Olga Markova. **B.** Examples of simulated trajectories (3h each) and filament positions for each scenario. Notice how contraction/extension dynamics of the filament allows it to sample the volume efficiently. **C.** Search times for three scenarios: cumulative distributions from simulations of Rouse trajectories, vertical lanes depict characteristic times estimated analytically, serving as good approximations of the median times from simulations. **D.** The median search time for the dynamic filament as a function of time spent in the extended state. Notice that a prolonged extended state can make the search less efficient. **E**. Polymer model of yeast chromosome organization, modeled following [34] (the nucleolus is shown in white, the filament in yellow). Search times and examples of trajectories (3000 s each) in the polymer model for no-filament and dynamic filament (filament is allowed to move, 28 frames shown) scenarios.

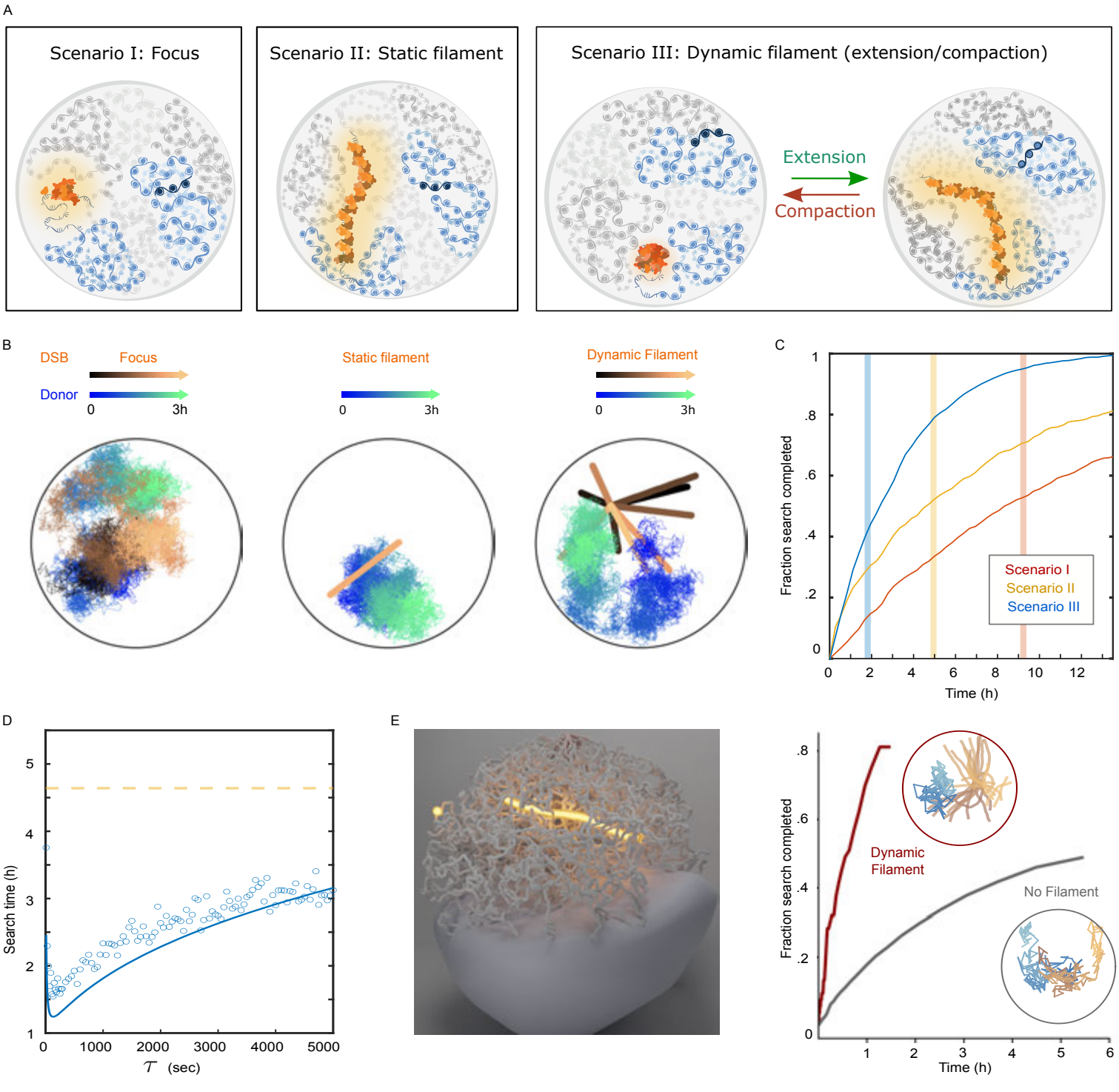
A
Scenario I: Focus
Scenario II: Static filament
Scenario III: Dynamic filament (extension/compaction)
Extension
Compaction
B
DSB
Focus
Donor
0
3h
Static filament
0
3h
Dynamic Filament
0
3h
C
Fraction search completed
Time (h)
Scenario I
Scenario II
Scenario III
D
Search time (h)
τ (sec)
E
Fraction search completed
Time (h)
Dynamic Filament
No Filament

References

1. Ait Saada, A., Lambert, S. A. E. & Carr, A. M. Preserving replication fork integrity and competence via the homologous recombination pathway. *DNA Repair* **71**, 135–147 (2018).
2. Wright, W. D., Shah, S. S. & Heyer, W.-D. Homologous recombination and the repair of DNA double-strand breaks. *J. Biol. Chem.* **293**, 10524–10535 (2018).
3. Kowalczykowski, S. C. An Overview of the Molecular Mechanisms of Recombinational DNA Repair. *Cold Spring Harb. Perspect. Biol.* **7**, a016410 (2015).
4. Barzel, A. & Kupiec, M. Finding a match: how do homologous sequences get together for recombination? *Nat. Rev. Genet.* **9**, 27–37 (2008).
5. Haber, J. E. DNA Repair: The Search for Homology. *BioEssays* **40**, 1700229 (2018).
6. Piazza, A. & Heyer, W.-D. Homologous Recombination and the Formation of Complex Genomic Rearrangements. *Trends Cell Biol.* **29**, 135–149 (2019).
7. Bonilla, B., Hengel, S. R., Grundy, M. K. & Bernstein, K. A. *RAD51* Gene Family Structure and Function. *Annu. Rev. Genet.* **54**, 25–46 (2020).
8. Sung, P. & Robberson, D. L. DNA strand exchange mediated by a RAD51-ssDNA nucleoprotein filament with polarity opposite to that of RecA. *Cell* **82**, 453–461 (1995).
9. Kong, M. & Greene, E. C. Mechanistic Insights From Single-Molecule Studies of Repair of Double Strand Breaks. *Front. Cell Dev. Biol.* **9**, 20 (2021).
10. Cejka, P. & Symington, L. S. DNA End Resection: Mechanism and Control. *Annu. Rev. Genet.* **55**, 285–307 (2021).
11. Lehmann, C. P., Jiménez-Martín, A., Branzei, D. & Tercero, J. A. Prevention of unwanted recombination at damaged replication forks. *Curr. Genet.* **66**, 1045–1051 (2020).
12. Carver, A. & Zhang, X. Rad51 filament dynamics and its antagonistic modulators. *Semin. Cell Dev. Biol.* **113**, 3–13 (2021).
13. Sun, Y., McCorvie, T. J., Yates, L. A. & Zhang, X. Structural basis of homologous recombination. *Cell. Mol. Life Sci.* **77**, 3–18 (2020).
14. Lesterlin, C., Ball, G., Schermelleh, L. & Sherratt, D. J. RecA bundles mediate homology pairing between distant sisters during DNA break repair. *Nature* **506**, 249–253 (2014).
15. Wiktor, J. *et al.* RecA finds homologous DNA by reduced dimensionality search. *Nature* **597**, 426–429 (2021).
16. Lisby, M., Barlow, J. H., Burgess, R. C. & Rothstein, R. Choreography of the DNA Damage Response: Spatiotemporal Relationships among Checkpoint and Repair Proteins. *Cell* 15 (2004).
17. Waterman, D. P. *et al.* Live cell monitoring of double strand breaks in S. cerevisiae. *PLOS Genet.* **15**, e1008001 (2019).
18. Essers, J. Nuclear dynamics of RAD52 group homologous recombination proteins in response to DNA damage. *EMBO J.* **21**, 2030–2037 (2002).
19. Berg, S. *et al.* ilastik: interactive machine learning for (bio)image analysis. *Nat. Methods* **16**, 1226–1232 (2019).
20. Miné-Hattab, J. & Rothstein, R. Increased chromosome mobility facilitates homology search during recombination. *Nat. Cell Biol.* **14**, 510–517 (2012).
21. Piazza, A. *et al.* Dynamic Processing of Displacement Loops during Recombinational DNA Repair. *Mol. Cell* **73**, 1255-1266.e4 (2019).
22. Jain, S., Sugawara, N., Mehta, A., Ryu, T. & Haber, J. E. Sgs1 and Mph1 Helicases Enforce the Recombination Execution Checkpoint During DNA Double-Strand Break Repair in *Saccharomyces cerevisiae*. *Genetics* **203**, 667–675 (2016).
23. Aylon, Y., Liefshitz, B., Bitan-Banin, G. & Kupiec, M. Molecular Dissection of Mitotic Recombination in the Yeast *Saccharomyces cerevisiae*. *Mol. Cell. Biol.* **23**, 1403–

1417 (2003).
24. Crickard, J. B., Moevus, C. J., Kwon, Y., Sung, P. & Greene, E. C. Rad54 Drives ATP Hydrolysis-Dependent DNA Sequence Alignment during Homologous Recombination. *Cell* **181**, 1380-1394.e18 (2020).
25. Hilario, J., Amitani, I., Baskin, R. J. & Kowalczykowski, S. C. Direct imaging of human Rad51 nucleoprotein dynamics on individual DNA molecules. *Proc. Natl. Acad. Sci.* **106**, 361–368 (2009).
26. Robertson, R. B. *et al.* Structural transitions within human Rad51 nucleoprotein filaments. *Proc. Natl. Acad. Sci.* **106**, 12688–12693 (2009).
27. Sung, P. & Stratton, S. A. Yeast Rad51 Recombinase Mediates Polar DNA Strand Exchange in the Absence of ATP Hydrolysis. *J. Biol. Chem.* **271**, 27983–27986 (1996).
28. Agmon, N., Liefshitz, B., Zimmer, C., Fabre, E. & Kupiec, M. Effect of nuclear architecture on the efficiency of double-strand break repair. *Nat. Cell Biol.* **15**, 694–699 (2013).
29. Batté, A. *et al.* Recombination at subtelomeres is regulated by physical distance, double-strand break resection and chromatin status. *EMBO J.* **36**, 2609–2625 (2017).
30. Gartenberg, M. R., Neumann, F. R., Laroche, T., Blaszczyk, M. & Gasser, S. M. Sir-Mediated Repression Can Occur Independently of Chromosomal and Subnuclear Contexts. *Cell* **119**, 955–967 (2004).
31. Gehlen, L. R., Gasser, S. M. & Dion, V. How Broken DNA Finds Its Template for Repair: A Computational Approach. *Prog. Theor. Phys. Suppl.* **191**, 20–29 (2011).
32. Miné-Hattab, J., Recamier, V., Izeddin, I., Rothstein, R. & Darzacq, X. Multi-scale tracking reveals scale-dependent chromatin dynamics after DNA damage. *Mol. Biol. Cell* **28**, 3323–3332 (2017).
33. Hajjoul, H. *et al.* High-throughput chromatin motion tracking in living yeast reveals the flexibility of the fiber throughout the genome. *Genome Res.* **23**, 1829–1838 (2013).
34. Arbona, J.-M., Herbert, S., Fabre, E. & Zimmer, C. Inferring the physical properties of yeast chromatin through Bayesian analysis of whole nucleus simulations. 1–15 (2017).
35. de Gennes, P. G. Kinetics of diffusion-controlled processes in dense polymer systems. I. Nonentangled regimes. *J. Chem. Phys.* **76**, 3316–3321 (1982).
36. Chupeau, M., Bénichou, O. & Voituriez, R. Cover times of random searches. *Nat. Phys.* **11**, 844–847 (2015).
37. Toczyski, D. P., Galgoczy, D. J. & Hartwell, L. H. CDC5 and CKII Control Adaptation to the Yeast DNA Damage Checkpoint. *Cell* **90**, 1097–1106 (1997).
38. Sandell, L. Loss of a yeast telomere: Arrest, recovery, and chromosome loss. *Cell* **75**, 729–739 (1993).
39. Sadeghi, A., Dervey, R., Gligorovski, V., Labagnara, M. & Rahi, S. J. The optimal strategy balancing risk and speed predicts DNA damage checkpoint override times. *Nat. Phys.* **18**, 832–839 (2022).
40. Challa, K. *et al.* Damage-induced chromatome dynamics link Ubiquitin ligase and proteasome recruitment to histone loss and efficient DNA repair. *Mol. Cell* **81**, 811-829.e6 (2021).
41. Dion, V., Kalck, V., Horigome, C., Towbin, B. D. & Gasser, S. M. Increased mobility of double-strand breaks requires Mec1, Rad9 and the homologous recombination machinery. *Nat. Cell Biol.* **14**, 502–509 (2012).

Methods:

Design of the Rad51 GFP insert

A multiple sequence alignment of *S. cerevisiae* Rad51 (RAD51_YEAST) was generated using HHblits against the UniRef30 database [42] and secondary structure were predicted using PsiPred from this MSA [43]. A structural model of full-length Rad51 was generated using the RaptorX server (Kallberg *et al.*, 2012) and used as a basis to map the evolutionary rates which were estimated using the Rate4Site algorithm [44] and the Rad51 MSA. Secondary structure predictions obtained from the RaptorX server suggests that the N-terminal end of *S.c.* Rad51 harbors some helical propensities with a few positions slightly conserved. These features could be due to functional constraints that account for the poor functionality of the N-terminal tagged versions of Rad51 tested so far. To identify a more favorable insertion site, we analyzed the MSA looking for a more flexible and variable region. The site between Gly54 and Gly55 fulfilled these criteria and a first version of a tagged Rad51, named Rad51-iGFP1, was generated using two 11-residues flexible linkers flanking the GFP of sequence 'GGAGSAGGAGG-GFP-GGAGSAGGAGG'. The promising results obtained for that first construct prompted us to further optimize the sequence of the linkers. We reasoned that to reduce as much as possible the influence of the acidic tag on the properties of the Rad51 filament, we could increase further the length of the linker and add positively charged residues in the vicinity of the GFP-tag. This led to the design of the Rad51-iGFP2 construct with two 16-residues flexible linkers with the following sequence 'GGAGSAGGAGNRKRNG-GFP-GNRKRNGAGSAGGAGG'. The structural model of the filament was built using the structure of *S.c.* Rad51[45] (PDB: 1SZP). The Pymol software was used to draw the different structures [PyMOL, The PyMOL Molecular Graphics System, Version 2.0 Schrödinger, LLC].

Strain and plasmid construction

All strains are derivatives of W303 [46]. Gene deletions, insertions of alternative promoters and gene tagging were performed by PCR-base gene targeting, except Rad51-iGFP strains. For Rad51-iGFP strains, the internal tagging of Rad51 between the 54th and 55th amino acid was obtained using the CRISPR-Cas9 technique. A guide rDNA obtained by hybridization of primers oAT2449 and oAT2450 was inserted into the pRS425-Cas9-2xSap1 (Kind gift of Bruce Futcher, State University of New York, Stoney Brook) yielding pAT569. The Rad51-iGFP strains were obtained by co-transformation of pAT569 together with a donor sequence that contained *RAD51* homologous sequences on either side of a fluorescent tag flanked by identical

linkers (11 amino acids for the Rad51-iGFP1 and 16 amino acids for Rad51-iGFP2). The donor for the Rad51-iGFP1 strain was generated by PCR on the yeGFP sequence of pYM25[47] with primer oAT2334 and oAT2335. The donor of the Rad51-iGFP2 strain was generated by PCR on pAT624 (a fragment of Rad51-isfGFP: synthetic construct from Genescript, this study) with primer oAT558 and oAT2401.

List of strains and primers used in this study can be found in Supplemental Table 1 and 2.

Viability assay

Strains were grown overnight in YPD and plated in fivefold serial dilutions starting at OD_{600nm}=1 on YPD plates containing 0%, 0.005%, 0.01% and 0.02% MMS (Methyl methanesulfonate). Plates were then incubated at 30°C for 48h.

Gene conversion experiment

Strains were grown overnight in YPA+3%Raf medium, and diluted to $OD_{600nm}=10^{-4}$. 100µl culture (corresponding to 100 cells) was plated separately on YPD and YP 2% galactose plate for 48h incubation at 30°C. Gene conversion efficiency was calculated by the number of colonies on YP-Gal plate divide by the corresponding number on YPD plate.

Immunofluoresence

A total of 20 OD_{600nm} equivalent cells was fixed in 0.9% paraformaldehyde (Sigma-Aldrich) and incubate at 30°C for 15min. Samples were centrifuged (12700 x g), washed twice with H_2O, and resuspended in 1.25ml solution (0.1M EDTA-KO, 10mM DTT, pH=8.0) for 30 min incubation with a gentle agitation. After centrifugation, the pellets were resuspended in 1.25ml YPD-Sorbitol (1.2M) and 15µl zymolyase-100T. Cells were incubated at 30°C and their shape was checked every 5 min by microscopy (transmitted light). The reaction was stopped by adding 40ml YPD-Sorbitol when cells became round and didn't reflect anymore. The spheroplasts were washed twice with YPD-Sorbitol and finally resuspended in YPD without sorbitol. Cells were dropped on microscope slides (Polylabo, super-teflon slides) and air dried for 3 min. Then, slides were put in methanol for 6 min and acetone for 30s at -20°C. After 3min air dry, the slides were incubated in 1xPBS with 1%BSA and 0.1%Triton X-100 for at least 20 min. Spots were covered by 1xPBS with 0.1% Triton X-100, anti-Rad51 antibody (PA5-34905 ThermoFischer, 1/500), and 1h incubation at 37 °C. After 3 washes in 1xPBS with 0.1% Triton X-100, the slides were dried and covered by Invitrogen goat anti-rabbit IgG(H+L) cross-

adsorbed secondary antibody (Alexa fluor 568, catalog #A-11011, 1/100 in spheroplast suspension). After 1h incubation at 37°C and three times wash with 1xPBS,0.1% Triton X-100, nuclei were dyed with 1x DAPI (in 1xPBS) for 5min. After 2 washes with 1xPBS, 15µl antifading (DABCO, pH7.5) was added to each spot. Slides were covered with a cover slip and stored at 4°C in the dark.

Western blot.

Cell lysates were extracted by the TCA method and 10min vigorous vortex at 4°C. After centrifuging (13,000 x g), the pellets were resuspended in TCA-Laemmli loading buffer (120 mM Tris base, 3.5 % sodium dodecyl sulfate (SDS), 8 mM EDTA, 5 % β-mercaptoethanol, 1 mM PMSF, 15 % glycerol, 0.01 % bromophenol blue). Samples were incubated at 95°C for 10min. For immunoblotting, a polyclonal antibody anti-Rad51 (PA5-34905 ThermoFischer) was used at 1:3000.

ChIP and quantitative PCR analysis

A total of 20 OD_{600nm} equivalent cells was fixed in 0.9% formaldehyde for 15 min at 30°C, and quenched with 0.125M glycine for 5 min. The following steps were done at 4°C, unless indicated. After washing in cold 1x TBS, the pellets were resuspended in 1 mL 1x TBS. After a second centrifugation at 12,000 x g, the pellets were frozen in liquid nitrogen and stored at -80°C. The pellets were suspended in 500 µl cold lysis buffer (0.01% SDS, 1.1% Triton X-100, 1.2 mM EDTA pH8, 16.7mM Tris pH8, 167mM NaCl, 0.5% BSA, 0.02 g/L tRNA, and 2.5 µl of protease inhibitor from Sigma-Aldrich P1860, Sigma-Aldrich, St. Louis, MO, USA), then 500µl 0.5mm zirconium beads were added. Cells were broken usingFASTPREP (MPBiomedicals) machine with maximum intensity for 30s, repeated 3 times with 3 min pause on ice. Samples were incubated 10min on ice and sonicated by Biorupter XL (Diagenode) for 14 min, high power with on and off cycles 30s. The extracts were centrifuged for 5 min at 12,000 x g. 10µl supernatants were kept at -20°C as input, while 2µl polyclonal antibody anti-Rad51(PA5-34905 ThermoFischer) were added into the remaining lysates overnight incubation. The next day, 50 µL of magnetic beads protein A (NEB) was added to the extracts / antibody mixture and incubated for 4 h at 4 °C on a rotating wheel. Then, the magnetic beads with the immunoprecipitated material were washed sequentially once with lysis buffer, twice with RIPA buffer (0.1% SDS, 10 mM Tris pH 7.6, 1 mM EDTA pH8, 0.1% sodium deoxycholate, and 1% Triton X-100), twice with RIPA buffer supplemented with 300 mM

NaCl, twice in LiCl buffer (250 mM LiCl, 0.5% NP-40, 0.5% sodium deoxycholate), once with 1× TE 0.2% Triton X-100, and a final was in 1× TE. The beads were then resuspended in 100 µL of elution buffer and placed in an incubator at 65 °C with gentle agitation to elute the immunoprecipitated material from the beads. In the meantime, the inputs were diluted 1/10 with elution buffer. A reversal cross-linking was performed by heating the samples, inputs and IP, overnight at 65 °C. Proteins were digested with Proteinase K (0.4 mg/mL) in the presence of glycogen, and the remaining DNA was purified on QIAquick PCR purification columns. Finally, samples were treated with 29 µg/mL RNase A for 30 min at 37 °C and used for quantitative PCR.

ChIP quantification was performed by quantitative PCR (qPCR) either on the 7900HT Fast Real-Time PCR (Applied Biosystems, Waltham, MA, USA) or on the QuantStudio 5 Real-Time PCR System (Applied Biosystems, Waltham, MA, USA). Sequences of interest were amplified using the SYBR Green PCR Master Mix (Applied Biosystems, Waltham, MA, USA) and the primers listed in Supplementary Table S2 on a dilution of immunoprecipitated DNA at 1/40 and 1/80 for the input DNA. PCR reactions were conducted using the following program: an initial denaturation at 95 °C for 10 min followed by 40 cycles (95 °C for 15 s and 60 °C for 30 s). Each real-time PCR reaction was performed in triplicate. The signal from a given region was normalized to the one from the OGG1 control locus in immunoprecipitated and input DNA samples. Plots represent the mean value obtained for at least three independent experiments and normalized by WT, error bars correspond to the SEM.

Microscopy

Yeast cells were grown in rich medium (YPD) overnight to early log-phase. To induce a single DSB at the I-*Sce*I cut-site, cells were grown overnight in YPA Raf3% medium (yeast extracts, peptone, 3% Raffinose, 0.008 % Adenine HCl) and diluted to OD_{600nm}=0.2 the next morning in the same medium. After 2h, galactose was added directly to the culture to reach a final concentration of 2%. Before microscopy, cells were rinsed with complete synthetic medium (2x final concentration pf CSM, MPBIO-101) and 3% Raffinose and placed on a 1.4% agarose patch for microscopy. For all fluorescent images, images were acquired in 3-dimensions with a z-step of 200nm: images shown are a maximum intensity projection of the z-stack images. Images were acquired on an inverted wide-field microscopy (Nikon TE2000) equipped with a 100x/1.4 NA immersion objective and a C-mos camara. A xenon arc lamp (Sutter Instrument Co. Lambda LS) and a spectra X light engine lamp (Lumenor) were used to illuminate the samples.

Time-lapse microscopy

For time-lapse microscopy, cells were grown overnight in complete synthetic medium (2x final concentration of CSM (yeast nitrogen base; MP Biomedicals) supplemented with 3% Raffinose. Cells were diluted to OD_{600nm}=0.2 the next morning in the same medium. After 2h, galactose was added directly to the culture to reach a final concentration of 2%.

50µl of cells with OD=0.4 (diluted in the original filtered medium) were transferred to the microfluidic yeast plate (CellASIC Onix, using Y04C-02-5PK plates for haploid strains: and Y04D-02-5PK plates for diploid strains). The plates were driven by the Onix microfluidic perfusion system. We loaded the cells into the chamber in 15s = and set the flow pressure at 13.8kPa (2psi) during acquisition.

Time-lapse movies were acquired on a spinning-disk confocal microscopy equipped with a spinning-disk unit (Yokogawa CSU-X1), a Nikon Ti2000 statif, a 100x/1.4NA oil immersion objective and an EM CCD camera (ANDOR iXON DU-8850). The microscope is driven by MetaMorph software, and images were acquired every 2 or 5 minutes in 3-dimensions with z-steps spaces by 300 nm. The images shown in the figures are maximum intensity projections of the z-stacks.

Quantification of filament length

Filaments were cropped to 50x50 pixel size images and deconvolved using the Meinel algorithm in MetaMorph (eight iterations; sigma =0.8; frequency 3; MDS Analytical Technologies). The length quantifications were performed in 3-dimensions using a home-made macro: the segmentation is based on an automatic image thresholding using the Ostu method.

The intensity of the filaments was calculated after segmentation of the sum-projection images. All programs are available as supplementary material.

Alignment of 2-color images

To align 2-colors images (GFP and RFP), we used a strain harboring the SPB tagged with 2 different proteins (green:SPC110-YFP::HIS3; red:SPC42-mCherry::KanMX) to estimate the shift between the 2 channels. Images from panel 1-H and supplementary figure 3 were aligned using this method.

Quantification through machine learning

2 ilastik (1.3.2 post1) projects were used to quantify the percentages of Rad51 structures, using a pixel and an object classification. At least 10 images were used for training. After

segmentation on z-projection images, simple threshold (0.44, with 0.7 and 0.7 smooth) was applied on nuclei to count the total number of nucleus. Hysteresis threshold (core 0.7, final 0.85, smooth 0.5 and 0.5) was done on nucleus as well as Rad51 signal to classify Rad51 structures. Object features (shape, diameter, length of skeleton and intensity distributions) were used in both projects.

For intensity quantification, 3D filaments stacks (50x50 pixel) were input and possessed by a simple threshold (0.6, with 0.8 and 0.8 smooth). Size in pixels, mean intensity and total intensity were chosen for classification and output.

Models of search

In this section we estimate times of homology search using both simple theory and simulations. We consider the following three mechanisms of search: (1) two compact chromosomal loci search for each other within the nuclear volume; (2) one compact chromosomal locus and a static filament; and (3) one locus and a dynamic filament. In all cases we assume that compact loci are much smaller than the nuclear volume (~50-100nm), and move with the Rouse diffusion, further confined within a spherical nuclear volume. Rouse diffusion $MSD = At^{0.5}$ of chromosomal loci have been now well-established in yeast and multicellular organisms [32,33,48–50], yielding in yeast $A_{2D} = 0.0055 - 0.01 \approx 0.0065\ \mu m^2/s^{1/2}$ (both before(*2*) and after DSB [20,32,33,41]) for 2D projections and hence $A = 3/2\ A_{2D} \approx 10^{-2}\mu m^2/s^{1/2}$ that we are using in theory and simulations (see Limitations for discussion of the accelerated movement after DSBs). Use of the Rouse dynamics not confined by other factors (beyond the nuclear volume) is further motivated by the relaxation of confinements after DSB [20,41]. A simple approach developed here aims at capturing the phenomenon of search facilitation by dynamic filaments, and hence the exact value of effective diffusion coefficient A and prefactors can only affect numerical estimates, but not the main result of significantly facilitated search.

Theory

We base our theory on a widely-used De Genne's argument [35] that the search by compact exploration proceeds through an increase in the volume being explored growing with time, and ends when the whole volume of the systems becomes explored, i.e. when the explored volume equals the volume of the system [51–55]. For a compact exploration process with $MSD = At^{\alpha}$ $(\alpha < 2/3\ for\ 3D)$, the explored volume is $V_{explored} \sim r^3 \sim MSD^{3/2} \sim t^{3\alpha/2}$, and the search proceeds until the whole volume of the nucleus $V_{nucleus} \sim R^3{}_{nucleus}$ is explored.

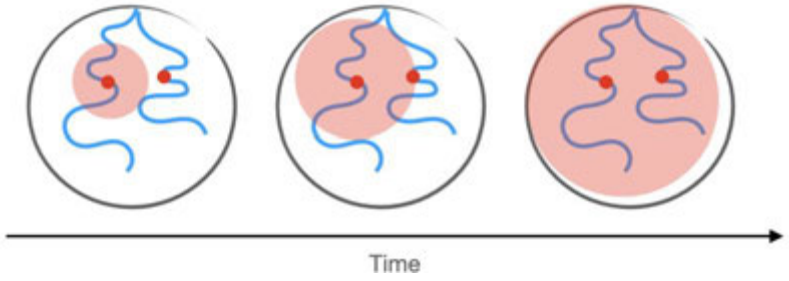

(1) *Two-loci search*. First we estimate the search time for a single Rouse searcher ($MSD = At^{0.5}$) looking for for an immobile target, i.e.

$V_{nucleus} = 4/3\pi R^3{}_{nucleus} = V_{explored} = 4/3\pi \Delta r^3 c = 4/3\pi MSD^{3/2} c = 4/3\pi c A^{3/2} t^{3/4}$, where a coefficient *c* reflects the fact that starting with a random position within a nucleus the explored volume, if spherical, would cover only a part of the nuclear volume when the volumes equal, and since trajectories reflected from the boundary are likely to cover already explored space, a factor of c larger volume needs to be explored. A sphere centered uniformly randomly within another one of the same radius overlaps by about 0.5 of its volume, suggesting $c \approx 2$. This yields an estimate, $t_{1\ searcher} \approx 2\ R^4_{nucleus}/A^2$, which agrees well with simulations for this case (**median**$(t_{1\ searcher})$=67,000sec, c=1.74). We crudely estimate that the search for two independently moving searchers would be approximately twice faster. Indeed, for each searcher, the other one is akin to an immobile target that can be found anywhere uniformly within the volume. Hence, we can approximate this by just asking what is the minimum of two search times. Since the Rouse search time is distributed approximately exponentially [51,54], we take the minimum of the two exponential random numbers (with the same rate) which is an exponential random number with twice the rate, hence we divide the 1-searcher time by half. This agrees with simulations which show that two moving searchers find each other approximately 1.7 times faster than one moving and one immobile.

This argument yield: $t_{2\ searchers} \approx R^4_{nucleus}/A^2$; using measured $A \approx 10^{-2}\mu m^2/s^{1/2}$ and $R_{nucleus} \approx 1.4\mu m$ we obtain **the search time**

$t_{2\ searchers} \approx R^4_{nucleus}/A^2 \approx 38{,}400\ s \approx$ **10.7h**

This estimate is in very good agreement with Rouse search simulations for two searcher that gives:

Mean **46,000sec** and Median **32,000sec ≈ 8.8h**

(see Supplemental Table 3 for confidence intervals and effects of parameters). Note that this is probably an underestimation of the search time for two compact loci as a number of factors can further constrain the dynamics (see below)

(2) *Search by the stable filament*. In this scenario, one of the loci is extended into a filament, while the other remains a compact locus. In this scenario, we assume that the filament is immobile and only the compact locus is performing a search. We also assume that the search ends once the searchin locus touches the filament anywhere along its length, i.e. we assume that the complementarity between the compact locus and the extended filament can be established at any point along the filament. Indeed, rephrasing famous Brouwer fixed-point theorem [56], if the sequence of the compact locus is complementary to that of the extended filament, no matter where the compact locus touches the filament there is going to be a sequence fragment within the compact one that is complementary to the site of the filament that is being touched.

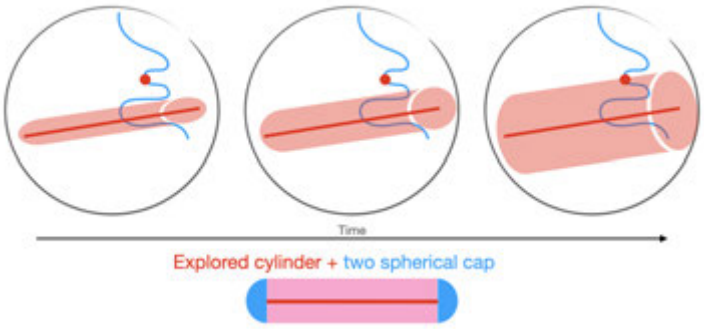

Then one can consider *the explored volume* as the volume *starting from where* the Rouse searcher can reach the filament in time *t.* Since in time *t* the locus displaces by $\Delta r(t) = MSD^{1/2} = A^{1/2}t^{1/4}$, the *explored volume* will then constitute a cylinder of radius $\Delta r(t)$, capped by semispheres of that radius, around the filament. The semispheres represent volumes around filament tips from where the searcher can travel to touch the tips. The logic stays the same for more complex organization of the filament: circular ones may not have the tips, but have larger L, branched ones would have more tips. Here for simplicity and due to its experimental prominence we consider the linear filament. Hence we obtain the explored volume as

$$V_{explored}(t) = \pi L \Delta r^2(t) + 4/3\pi \Delta r^3(t) = \pi L MSD + 4/3\pi MSD^{3/2}$$
$$= \pi L\, At^{1/2} + 4/3\pi A^{3/2}t^{3/4}.$$

As above, the search ends once the explored volume reaches the nuclear volume ($V_{explored}(t) = V_{nucleus}$) (i.e. a locus that started the search anywhere within the nuclear

volume would reach the filament). The search time can be found by solving the cubic equation for variable $y = t^{1/4}$:

$$4/3\pi\, R^3{}_{nucleus} = \pi L\, At^{1/2} + 4/3\pi A^{3/2} t^{3/4};$$

$$R^3{}_{nucleus} \approx LAt^{1/2} + A^{3/2} t^{3/4}$$

$$A^{3/2} y^3 + LAy^2 - R^3{}_{nucleus} = 0$$

For experimentally measured $R_{nucleus} \approx 1.4\mu m$ and taking $L \approx 1.2\mu m$ (at 4h) this approach yield the search time of

$$\boldsymbol{t_{stable\ filament} \approx 17{,}800\ \text{sec} \approx 4.5\text{h}}$$

which is very close to the results of simulations of such search dynamics:

Mean ≈ 28,000 sec Median ≈ 17,800sec ≈ 4.5h

Note that a static filament provides only about 2-3 fold reduction in the search time compared to the two-loci search. Critical for this facilitated search is the increase on the surface area of the searcher through formation of the filament: the longer filamentous structure the more significant is the acceleration.

(3) *Dynamics filament search*. One can extend the approach developed for the stable filament to a dynamic that experiences cycles of extension and compaction. Using an approach developed for 3D/1D search of proteins for their sites on DNA [57], we consider the search process as consistenting from consecutive cycles of search. During each such cycle, the filament is formed for some characteristic period of time τ , after which it compacts and stays in the compact state for τ_0, and then extends again. During each extended phase, the filament is not moving, while each extension starts at a random nuclear location -- together these capture high mobility of the filament we observe in microscopy. If the filament is only accessible for searchers for time τ, searchers from the volume $V_{explored}(\tau)$, defined in the previous section, can reach the filament.

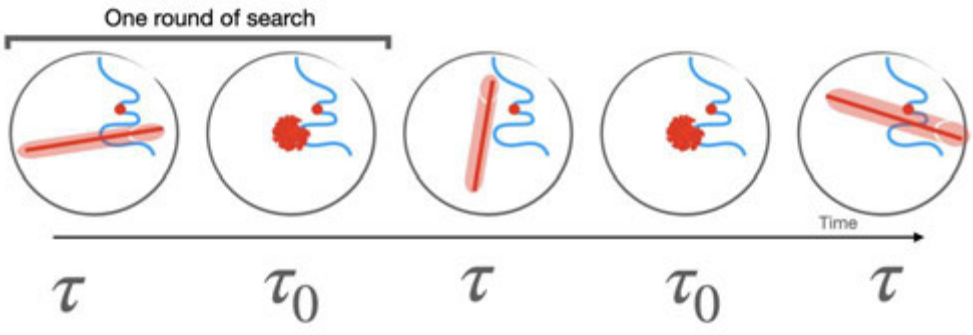

Hence, the probability of having a successful search in a given round is the probability that the searcher is located with the volume explored during this round, i.e. $p_{success} = V_{explored}(\tau)/V_{nucleus}$, assuming that each time an independent volume is explored.

If the probability of success on each round is $p_{success}$, the mean number of rounds required to achieve successful search is then $1/p_{success}$, and using the time each round takes is $\tau + \tau_0$, we obtain the mean search time as

$$t_{dynamic\ filament} = 1/p_{success}(\tau + \tau_0) = V_{nucleus}/V(\tau)_{explored}\ (\tau + \tau_0),$$

where $V_{explored}(t)$ for a linear filament is given above. Since the target is found during the last round of search, only about half of the time of the last round contributes to search, leading to a more accurate expression:

$$t_{dynamic\ filament} = 1/p_{success}(\tau + \tau_0) = [V_{nucleus}/V(\tau)_{explored} - 1/2]\ (\tau + \tau_0),$$

Figure 4 shows a good agreement between the search time computed this way and simulations as a function of τ. One can see that the fastest search can be achieved for $\tau \approx 2\tau_0$, with the coefficient 2 arising due to complex dependence of $V(\tau)_{explored}$ on τ. For experimentally measured $\tau = 1000\ sec; \tau_0 = 100\ sec$ and same geometric parameters as above one gets

$$t_{dynamic\ filament} = 6{,}500 sec \approx \mathbf{1.8h}$$

which is remarkably close to the search time seen for this mechanism in simulations.

Mean ≈ 11,700 sec Median≈ 9,360≈2.6h

Moreover, one can estimate the number of rounds needed to find the target as $V_{nucleus}/V_{explored}(\tau)$, yielding **7-8 rounds**.

Interestingly, from both theory and simulations we see that the search time is non-monotonic with τ, allowing to estimate the optimal τ/τ_0 ratio or compute optimal τ numerically. If one were to ignore the semispheres around filament caps and use $V_{explored}(\tau)$=$\pi L\ A\tau^{1/2}$, then $t_{dynamic\ filament} \sim\ \tau^{-1/2}(\tau + \tau_0)$, yielding the fastest search as a function of τ. This yields $\tau^{opt} = \tau_0$, i.e. when the filament time is partitioned 50/50 between extended and collapsed states. Using the full expression for $V_{explored}(\tau)$=$\pi L\ A\tau^{1/2} + 4/3\ \pi A^{3/2}\tau^{3/4}$ would give a different value for τ^{opt} that for values of L and A used, gives $\tau^{opt} \approx 1.2\ \tau_0$.

Experimental values deviate more from this optimal time partitioning ($\tau \sim 18min$ $\tau_0 \sim 2min$). However, having $\tau > \tau_0$ leads to only modest and gradual increase in the search time, while, on the contrary, $\tau < \tau_0$ leads to a dramatic increase in the search times, as for small tau the search becomes very inefficient and many more rounds of search are required. In vivo Rad51 filament has the lifetime above the optimal τ, but doesn't

Interestingly, facilitation of search due to dynamics of the filament is very similar to the mechanism of facilitated 3D/1D search by DNA-binding proteins. In both cases compact exploration (1D scanning along DNA or Rouse diffusion in search for a filament) is ineffective, requiring large jumps (3D diffusion or restructuring of the filament). The 3D/1D search time can be written as [57,58]

$t_{3D/1D\,search} = 1/p_{success}(\tau_{1D} + \tau_{3D}) = M/n(\tau_{1D})\,(\tau_{1D} + \tau_{3D})$, where is the total genome length (equivalent to the total volume to search) and $n(\tau_{1D})$ is the number of sites on DNA visited on each round of 1D diffusion that take τ_{1D} , and the time of each 3D flight is τ_{3D}. The optimal search is achieved when τ_{1D}=τ_{3D}. One can see that this expression is identical to the one for dynamic filament. Like for other intermittent search strategies, randomization on every round makes the search much more efficient.

Simulations of Rouse trajectories

The search is simulated as a Rouse diffusion in the spherical nucleus of radius $R_{nucleus}$. The trajectory is modeled as a fractal-Brownian motion (fBm) with 1sec discrete steps, such that $MSD \sim At^{1/2}$. Boundaries of the sphere are considered reflective, as recently introduced for fBms [59], but with a reflection in random direction, i.e. when a trajectory attempt to leave the sphere, the rest of the trajectory is rotated by a random angle, allowing it to continue inside the sphere (see Limitations, below). Loci are said to find each other if they approach each other closer than a distance cutoff d_{cutoff}=*50*nm. We tested cutoffs of 25 and 100nm, and, as expected theoretically [60], found that resulting search time changes by less than by 50%.

For the two-loci search, two fBm trajectories as simulated starting from random initial points within the nuclear volume. For a stable filament, the filament is being placed at a random nuclear position and points in a random direction, conditional on the other end being within the nucleus. For a dynamic filament, the origins and the orientation of the filament are being chosen at random at each round of search, *i.e.* after search for time τ, thus capturing a great deal of filament mobility we observe in microscopy. Each simulation run models the search for

$2x10^5$sec, 1000 such simulations are done for each scenario. This allows computing the mean, the median and the distribution of search times, the latter being very close to exponential, as known for Rouse search processes [51]. Obtained values of the search time are given in the Supplemental Table 4.

Full polymer model and simulation setup

Simulations were inspired by the Yeast model presented in (26). We employed a lab-written wrapper, around the open-source GPU-assisted molecular dynamics package Openmm to perform the simulations. Parameters were as described by Arbona et al. except for a duplication of chromosomes and a radius change from 1 µm to 1.5 µm to adapt the model to diploid yeast. The Rad51 filament was modeled in two ways depending on whether the rod was dynamic or static. Both rods were made from 100 15 nm beads, but the static rod was connected with angle potentials 374 times stiffer than the rest of the polymer while the dynamic rod had potentials 16 times lower---leading to a more realistic persistence length of 400 nm.

Before duplication, we ran simulations of the haploid system to calibrate length and time-scales. The length-scale was set by the bead size which was found match measured distances in haploid yeast with a root mean squared error of 101 nm (Fig. 1B). The timescale was set by comparison to mean squared displacement (MSD) measurements of the URA3 locus (4) where it was found that it took ~56 s to obtain an MSD of ~0.1 µm (Fig. 1B).

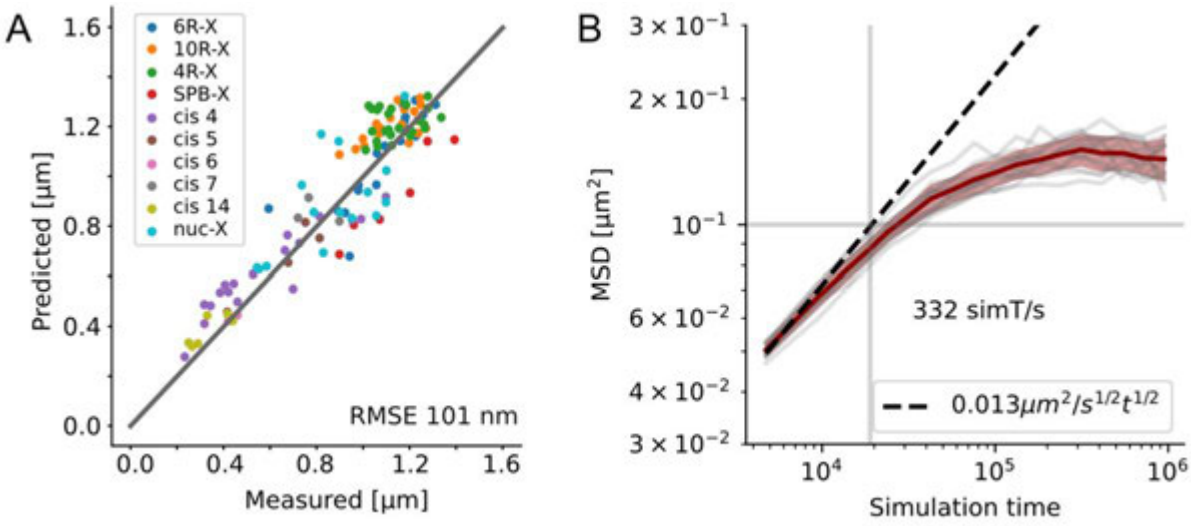

Distance and time calibration of the yeast polymer model. A: Comparison of equilibrium loci distances in simulation vs. measurements compiled in (26). The root mean squared error (RMSE) across all loci was found to be 101 nm (grey line denotes perfect agreement). B: Individual (grey) and averaged (red curve, shading is +- std. dev.) mean squared displacement (MSD) trajectories of loci reaching equilibrium MSDs similar to the URA3 locus of diploid yeast in (4). The conversion factor between simulation time (simT) and real time was identified as the ratio of the time to reach 0.1 μm which was experimentally found to be 56 s. The dotted line represents a characteristic anomalous diffusion coefficient of the locus.

Upon calibration and duplication, we performed long simulation to equilibrate the system after which several configurations were sampled to form the starting points for the search-simulations. Search pairs were defined as the locus closest to a randomly drawn point in a half sphere opposite the nucleolus and its homolog. For searches without a rod, 20 loci were followed in parallel to improve statics. The search was terminated when the homolog got within 3 bead radii (75 nm) of the locus or any bead in the rod. For dynamic searches, the rod was periodically removed after 1000s and re-inserted in a new direction after 100s to model the extension cycles suggested by experiments.

Factors that could potentially slow-down the search are the following.

(a) **Recognition of the locus may take some additional time.** Furthermore, when homology is incomplete, the donor sequence is sequestered by the decoy. This is likely less relevant for filaments as sequestration of any one part of the filament doesn't affect the rest of it allowing other regions to be accessed.

(b) **Sequestration by decoys can potentially prevent recognition on the first encounter**, making search taking longer. The filament provides an advantage by allowing simultaneous probing by multiple decoy donors that do not sterically occlude each other as much as they would for a compact DSB locus. Furthermore, even if occluded by the decoy, the DSB can be recognized by the donor after the decoy

dissociates. Due to the compact exploration, recognition of the second or third encounter is likely to immediately follow the first encounter. Also, recognition and rejections of decoy sequences were estimated to take the order of seconds, while the total search time being estimated is in tens of thousands of seconds. So, delay for a few seconds when the searcher arrives wouldn't slow down the global search process.

(c) **Similarly, the compacted states of the locus may require some time for the locus to detect homology**, potentially allowing it to dissociate without detecting it. As explained above, the compact nature of search provides multiple immediate encounters, allowing the searching locus to recognize its target from the second or third attempts.

(d) **Recognition may require a closer than 50nm approach of the locus to the filament.** Supplemental table shows that using 25nm instead of 50nm lead to at about 20-40% increase in the search time, arguing that this is not a very relevant parameter. Furthermore, 5Kb locus is expected to have the size (end-to-end distance) of ~100nm (ideal chain of 25 nucleosomes, with the persistence length of 5 nucleosomes gives $10nm * \sqrt{25 * 5} \approx$ 100nm). Using parameters from [34] ($60(bp/nm)$ of linear compaction and $80nm$ of the persistence length) we find that 5Kb locus would have the end-to-end distance of $\sqrt{5000bp/60(bp/nm) * 80nm} = 80nm$. Since the radius of gyration is sqrt(6)=2.4 smaller than the end-to-end distance, it yields the radius of gyration of **40nm** and **33nm** for 100nm and 80nm end-to-end distances correspondingly. Together this supports our estimate of 50nm contact distance.

(e) **Variable filament length.** We assumed the filament of a constant 1.2um in length, while experiments show that the average filament length changes from 0.9 at 2h to 1.3um at 4h, both broadly distributed in individual cells (Fig 2a). While shorter filaments make search by a static filament slower, dynamics of the filament is much less affected by this and remains fast 2.5h in simulations for L=0.9um. Moreover, the benefit of the dynamic filament becomes even more pronounced for shorter filaments.

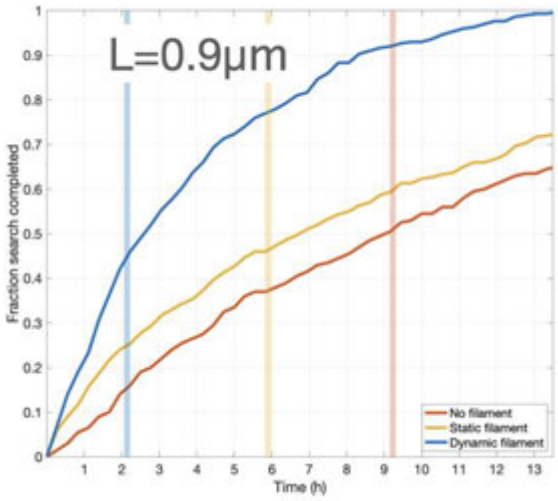

Factors that can potentially make search faster

(a) **Closer relative position of homologous loci that are equidistant from the centromeres**. This factor could potentially reduce the search time for the two-loci case , nevertheless the effect is going to be very modest. In fact, it was shown [60] that the search time scales linearly with the initial distance d between loci $t \sim d\ R^3/A^2$. Further moder Mine-Hattab et al provide extensive measurements of initial distances for *URA3* loci in diploid yeast cells, obtaining the mean approximately 1um. In our simulations the initial distance was random, which is approximately the radius of the sphere (1.4um). Using the linear scaling of the search time with initial distance suggests ~40% reduction in the search time.

(b) **Accelerated dynamics after the break**. An increased mobility after the DSB is hard to capture in a model since it doesn't represent neither a simple increase in A nor a change of α, but some combined and yet to be understood change in the mobility. One possibility is that such increase in mobility is due to the relaxation of some constraints (centromere attachments, linker length etc), but our theory and simulations already consider an unconstrained Rouse mobility. Another possibility is that Rad51-mediated dynamics captured here is the underlying source of increased mobility of a DSB proximal probe and other chromosomes.

(c) Dynamics and structure of the filament can significantly accelerate search. While fluctuations of the filament can increase the explored volume, more

complex shapes of the filament can significantly facilitate the search. For example, circular filaments with larger circumference can increase L. Branching ones in turn create more tips further increasing the "surface area" of the target for searchers. Continuously changing shapes can also explore the volume very efficiently.

Taken together these factors suggest that explicit simulations of the full polymer system may provide better estimates of the search time, at a cost of higher computational complexity and many additional parameters of the model. Further understanding the origin of accelerated dynamics after DSB can help take this phenomenon into account.

Statistics & Reproducibility

Western blots have been done for 4 times independently with similar results (Extended Figure1A). For quantification and image analysis, the acquisitions have been repeated at least twice for each condition independently. The specific n numbers is provided in the corresponding legend. The representative fluorescent images of Rad51-iGFP and 5 classes of Rad51 filaments (Figure 1D,3D and Extended Figure 4C) were selected among more than 20 independent acquisitions. The distribution of 5 classes and the representative filaments (Figure 3E, Extended Figure 7A,8A) were calculated and selected from 2 independent experiments. The Rad51 filaments localized by Immunofluorescence were selected from 3 different samples (Extended Figure 7B). The representative images of YFP-Rad51 and Rad51-GFP (C-terminal tag) strains (Extended figure 1B and 1C) are cropped from 10 different fields in 2 independent experiments. Hydroxyurea treatment has been repeated three times independently with different release time (Extended Figure 4A). Rad51-iGFP Nup57-mCherry strain has been observed three times (Extended figure 6B).

Statistical analyses were done through two-side Wilcoxon rank sum test (Matlab program) or two-sided Fisher's exact test (Prism9).

No statistical method was used to predetermine sample size. Sample sizes were chosen based on best practices in the field for experimental methods used. Dead or out-focus cells, and contaminated cultures are excluded in quantification on living cells. Unless otherwise stated, a minimum of 100 cells or 50 Rad51 structures was examined per condition and per experiment. The investigators were not blinded to allocation during experiments and outcome assessment. Therefore, to reduce potential human bias, the critical steps in the analysis were automated.

Data and materials availability: All data are available in the main text or the supplementary materials. Raw images presented in the manuscript are openly available in Zenodo under the DOI: 10.5281/zenodo.8104491. Strains and raw images quantified but not shown in the manuscript are available upon request.

Code availability

Codes for polymer model are available on : https://github.com/open2c/polychrom https://openmm.org/. Other codes are available in supplementary materials.

Methods only references

42. Remmert, M., Biegert, A., Hauser, A. & Söding, J. HHblits: lightning-fast iterative protein sequence searching by HMM-HMM alignment. *Nat. Methods* **9**, 173–175 (2012).
43. McGuffin, L. J., Bryson, K. & Jones, D. T. The PSIPRED protein structure prediction server. *Bioinformatics* **16**, 404–405 (2000).
44. Pupko, T., Bell, R. E., Mayrose, I., Glaser, F. & Ben-Tal, N. Rate4Site: an algorithmic tool for the identification of functional regions in proteins by surface mapping of evolutionary determinants within their homologues. *Bioinformatics* **18**, S71–S77 (2002).
45. Conway, A. B. *et al.* Crystal structure of a Rad51 filament. *Nat. Struct. Mol. Biol.* **11**, 791–796 (2004).
46. Thomas, B. J. & Rothstein, R. Elevated recombination rates in transcriptionally active DNA. *Cell* **56**, 619–630 (1989).
47. Janke, C. *et al.* A versatile toolbox for PCR-based tagging of yeast genes: new fluorescent proteins, more markers and promoter substitution cassettes. *Yeast* **21**, 947–962 (2004).
48. Oliveira, G. M. *et al.* Precise measurements of chromatin diffusion dynamics by modeling using Gaussian processes. *Nat Commun* **12**, 6184 (2021).
49. Gabriele, M. *et al.* Dynamics of CTCF- and cohesin-mediated chromatin looping revealed by live-cell imaging. *Science* eabn6583 (2022) doi:10.1126/science.abn6583.
50. Bronshtein, I. *et al.* Exploring chromatin organization mechanisms through its dynamic properties. *Nucleus* **7**, 27–33 (2016).
51. Yeung, C. & Friedman, B. Cyclization of Rouse chains at long- and short-time scales. *J. Chem. Phys.* **122**, 214909 (2005).
52. Dorfman, K. D., Fulconis, R., Dutreix, M. & Viovy, J.-L. Model of RecA-mediated homologous recognition. *Phys Rev Lett* **93**, 268102 (2004).
53. Doi, M. *Introduction to polymer physics*. (Clarendon Press, 1996).
54. Condamin, S., Bénichou, O. & Klafter, J. First-passage time distributions for subdiffusion in confined geometry. *Phys Rev Lett* **98**, 250602 (2007).
55. Amitai, A. & Holcman, D. Polymer physics of nuclear organization and function. *Phys Rep* **678**, 1–83 (2017).
56. Hazewinkel, M. *Encyclopaedia of Mathematics (1)*. (Springer, 1987).
57. Slutsky, M. & Mirny, L. A. Kinetics of Protein-DNA Interaction: Facilitated Target Location in Sequence-Dependent Potential. *Biophys. J.* **87**, 4021–4035 (2004).
58. Mirny, L. *et al.* How a protein searches for its site on DNA: the mechanism of facilitated diffusion. *J Phys Math Theor* **42**, 434013 (2009).

59. Guggenberger, T., Pagnini, G., Vojta, T. & Metzler, R. Fractional Brownian motion in a finite interval: correlations effect depletion or accretion zones of particles near boundaries. *New J Phys* **21**, 022002 (2019).
60. Condamin, S., Bénichou, O., Tejedor, V., Voituriez, R. & Klafter, J. First-passage times in complex scale-invariant media. *Nature* **450**, 77–80 (2007).

Extended data figures

Extended Data Figure 1: Rad51-iGFP is expressed at wild-type level and form filaments upon DSB induction, in contrast to N and C-tagged Rad51.

A. Western blot on WT and Rad51-iGFP strains at different time after DSB induction, rad51Δ is shown as negative control. **B.** Representative fluorescent images of YFP-Rad51 (from [16], N-terminal tag) and Rad51-iGFP after 2h Zeocin treatment, Z-projection is applied. **C.** Representative fluorescent images of Rad51-GFP (C-terminal tag) and Rad51-iGFP with I-SceI cutting site after 4h galactose induction, Z-projection is applied.

A

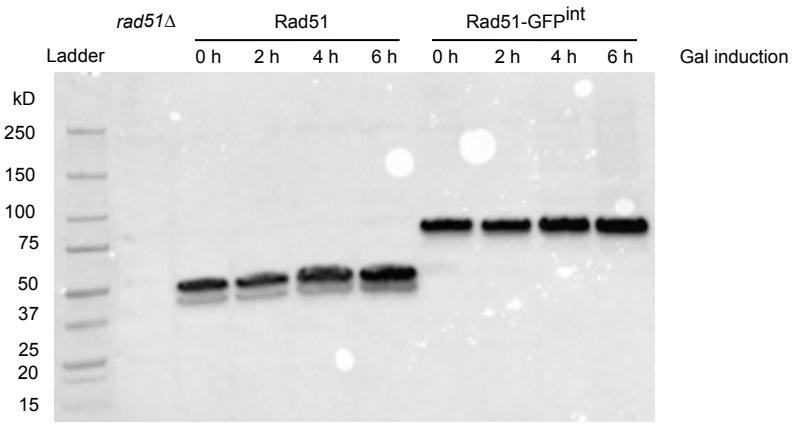
rad51Δ
Rad51
Rad51-GFPint
Ladder
0 h
2 h
4 h
6 h
0 h
2 h
4 h
6 h
Gal induction
kD
250
150
100
75
50
37
25
20
15

B

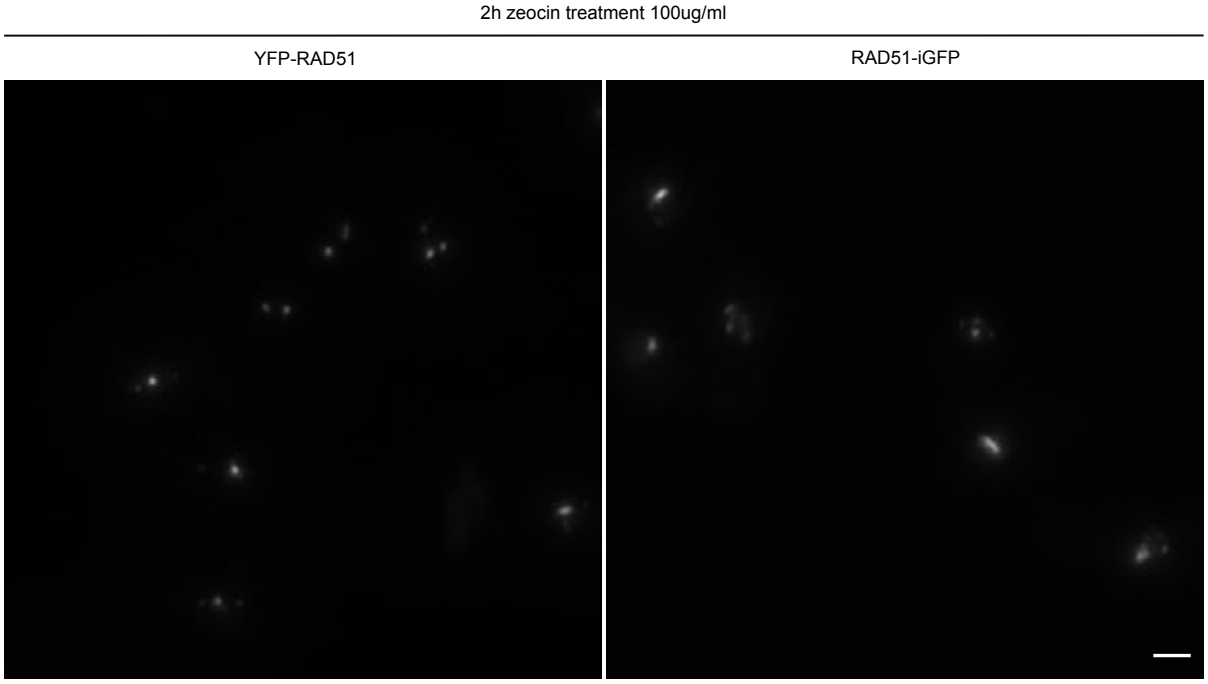
2h zeocin treatment 100ug/ml
YFP-RAD51
RAD51-iGFP

C

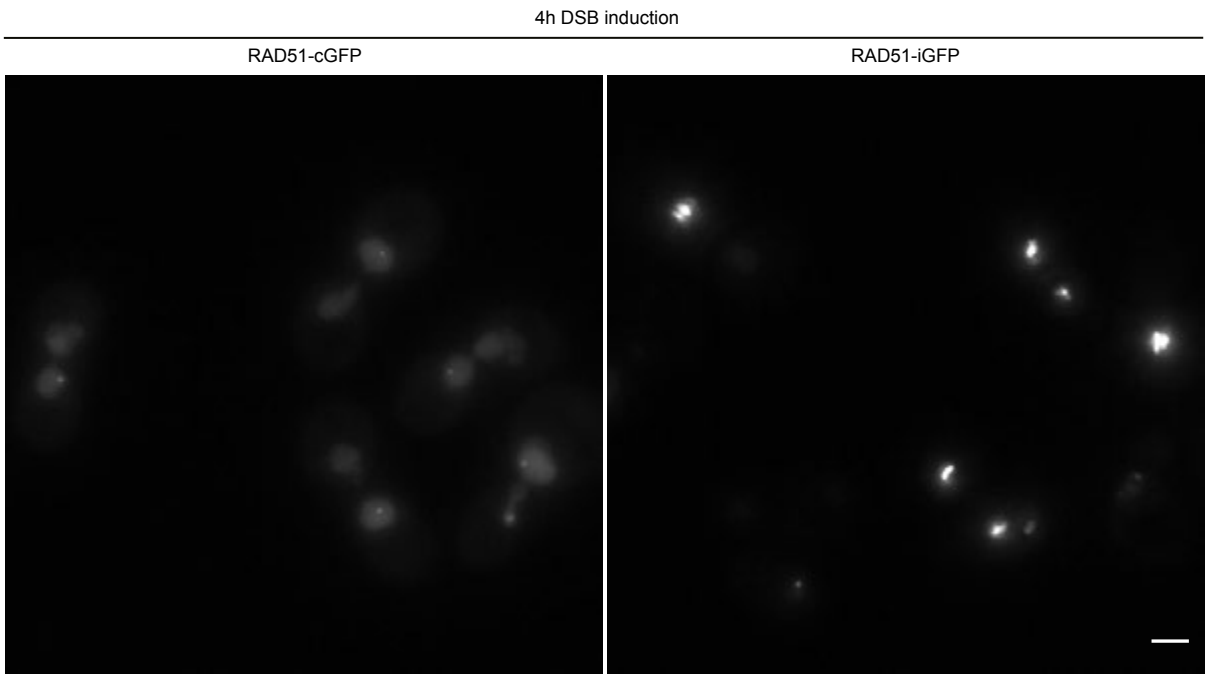
4h DSB induction
RAD51-cGFP
RAD51-iGFP

Extended Data Figure 2: Quantification methods and Rad51-iGFP in haploid and diploid strains.

A. Quantification of Rad51 structures using the machine-learning-based image analysis tool, Ilastik [19]. Input: Z-projection fluorescent images. Output: left, number of nuclei; right, numbers of Rad51 foci, globular structures, and filaments. **B.** Representative images fluorescent images of a Rad51-iGFP in haploid and diploid strain at different time after DSB induction maximal Z-projections are shown. **C.** Percentages of Rad51 foci, globular structures, and filaments at different time after DSB induction in haploid and diploid strains quantified as in D (n>100 cells examined per experiment, per condition with a total of n=2416 over 2 experiments, data are presented as mean values +/- SEM).

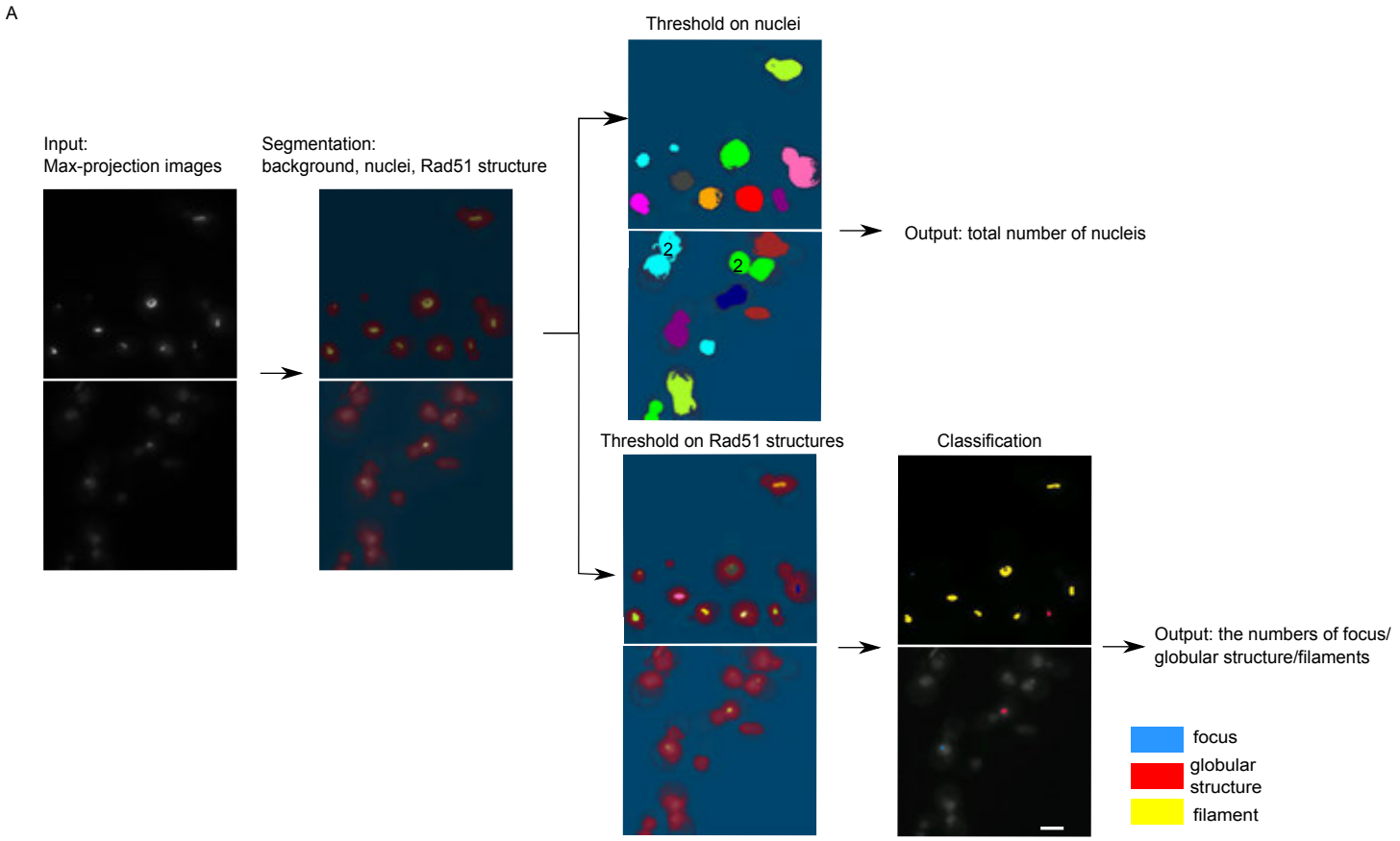
A
Input:
Max-projection images
Segmentation:
background, nuclei, Rad51 structure
Threshold on nuclei
2
2
Output: total number of nucleis
Threshold on Rad51 structures
Classification
Output: the numbers of focus/
globular structure/filaments
focus
globular
structure
filament

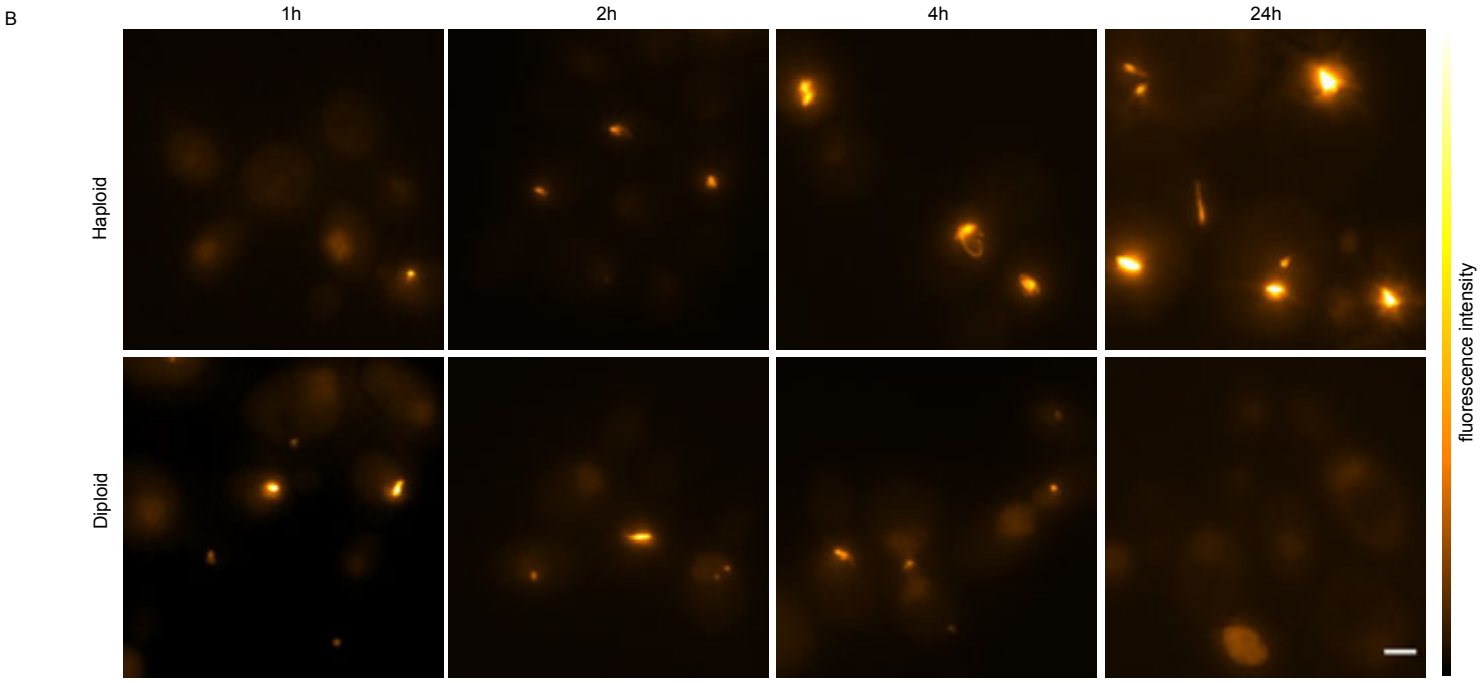
B
1h
2h
4h
24h
Haploid
Diploid
fluorescence intensity

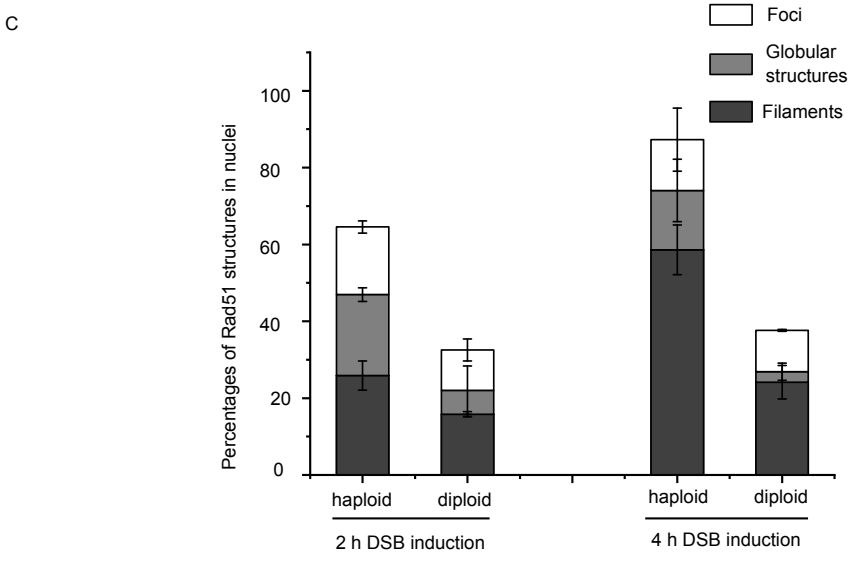
C
Foci
Globular
structures
Filaments
Percentages of Rad51 structures in nuclei
100
80
60
40
20
0
haploid
diploid
haploid
diploid
2 h DSB induction
4 h DSB induction

Extended Data Figure 3: Rad51-iGFP can form filaments in the presence of an intrachromosomal donor sequence.

A-B. Representative fluorescent images and percentages of Rad51-iGFP structures in the following strains after 2, 4 or 6h endonuclease induction: yAT4553 where HO creates a DSB at the *MATalpha* locus that can be repaired with the HM loci on the same chromosome (with a preference for HMR, located 90kb away from the cut site); yAT3880, where I-*Sce*I creates a DSB at the *lys2* locus in the absence of a donor sequence, yAT4552, where I-*Sce*I creates a DSB at the *lys2* locus in the presence of a donor sequence, 20kb upstream. maximal Z-projections are shown. (n>100 cells examined per experiment, per condition with a total of n=6670 cells examined over 2 experiments; data are presented as mean values +/- SEM).

A

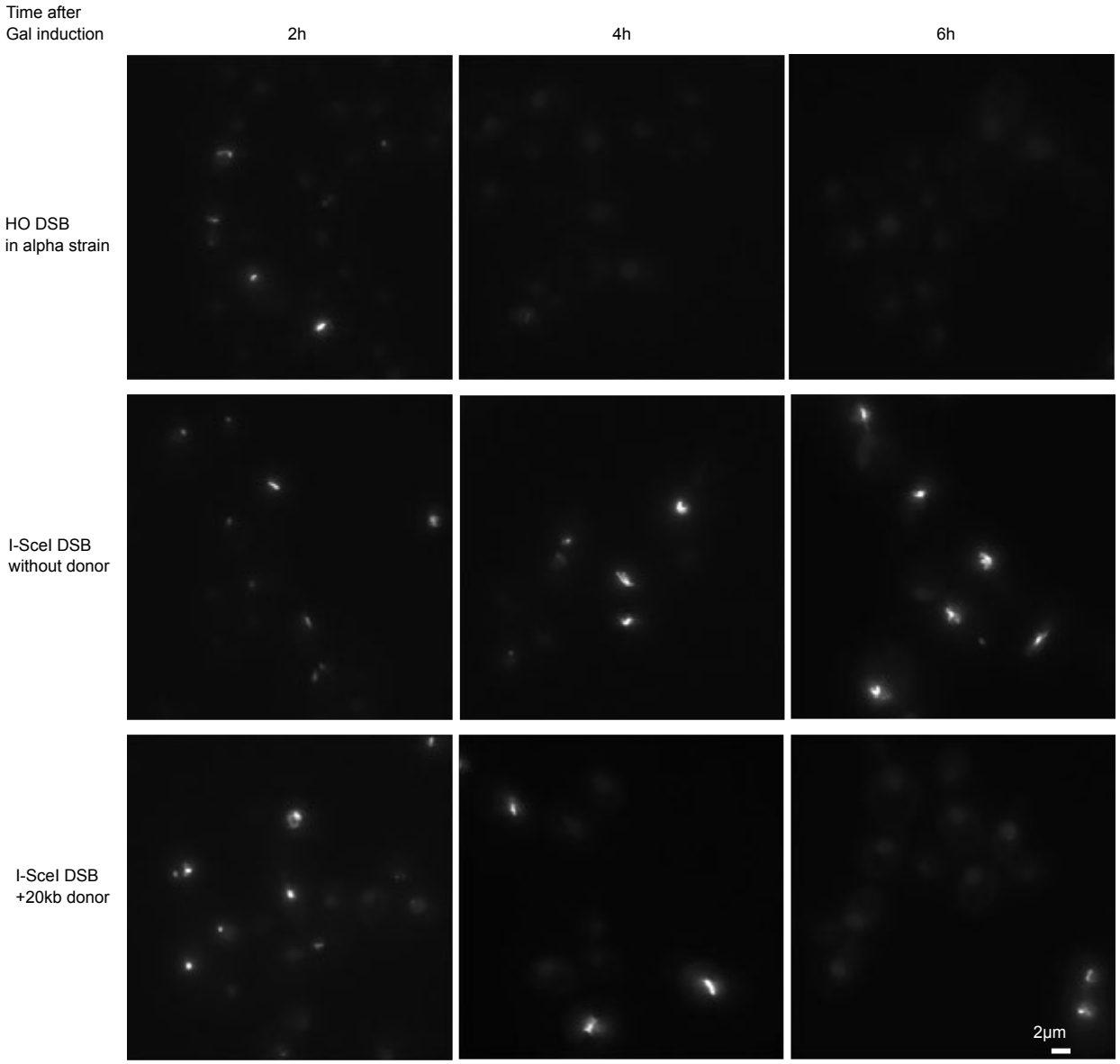
Time after
Gal induction
2h
4h
6h
HO DSB
in alpha strain
I-SceI DSB
without donor
I-SceI DSB
+20kb donor
2μm

B

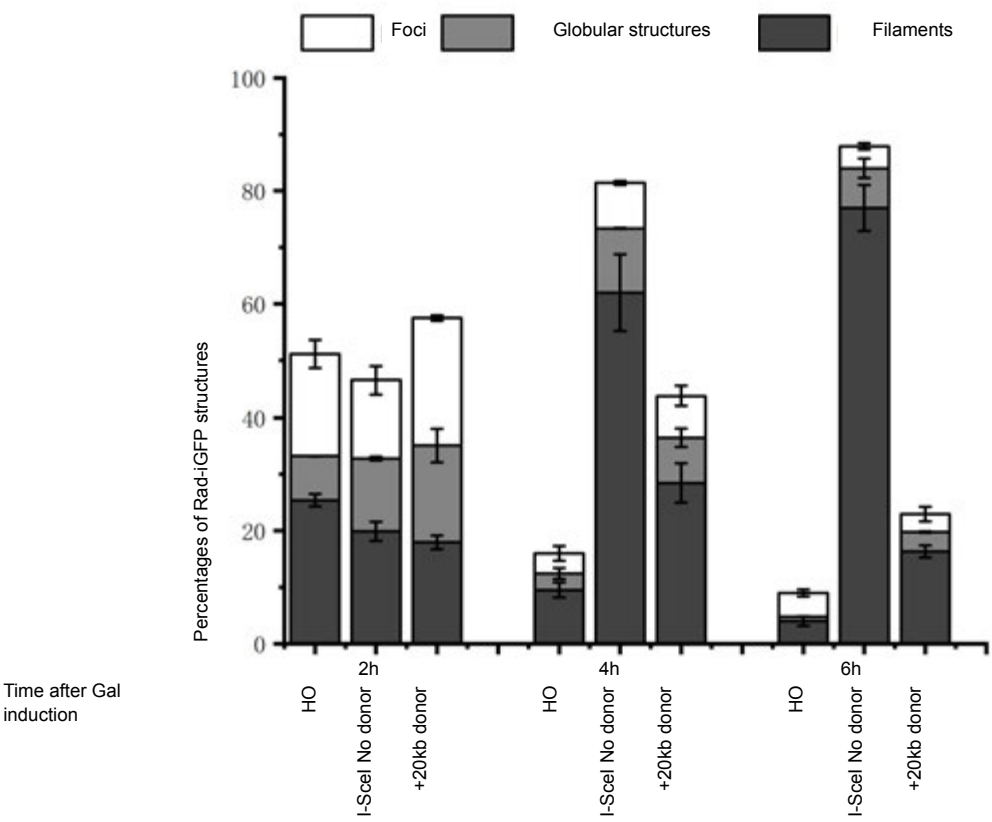
Foci
Globular structures
Filaments
Percentages of Rad-iGFP structures
100
80
60
40
20
0
2h
4h
6h
HO
I-SceI No donor
+20kb donor
Time after Gal
induction

Extended Data Figure 4: Rad51-iGFP upon replication stress and prolonged G1 synchronization

A. Representative fluorescent images of Rad51-iGFP after 1, 2, 3 h release from 1 h 200mM hydroxyurea treatment, Z-projection is applied. **B.** Representative images (Transmitted-light image, fluorescent image, and merged image) of Rad51-iGFP with I-*Sce*I cutting site after 2 h galactose induction. Cells that are unambiguously in G1 phase, as attested by the absence of a bud, are circled. Z-projection is applied. **C.** Schemes for G1 synchronization and galactose induction, 10μM alpha factor is induced at the beginning of synchronization and every 30min after galactose induction. Representative images (Transmitted-light image and fluorescent image) and percentages of Rad51 structures of Rad51-iGFP with I-*Sce*I cutting site after 3 h galactose induction under alpha factor arrest or release, maximal Z-projections are shown.
Scale bars: 2 μm.

A

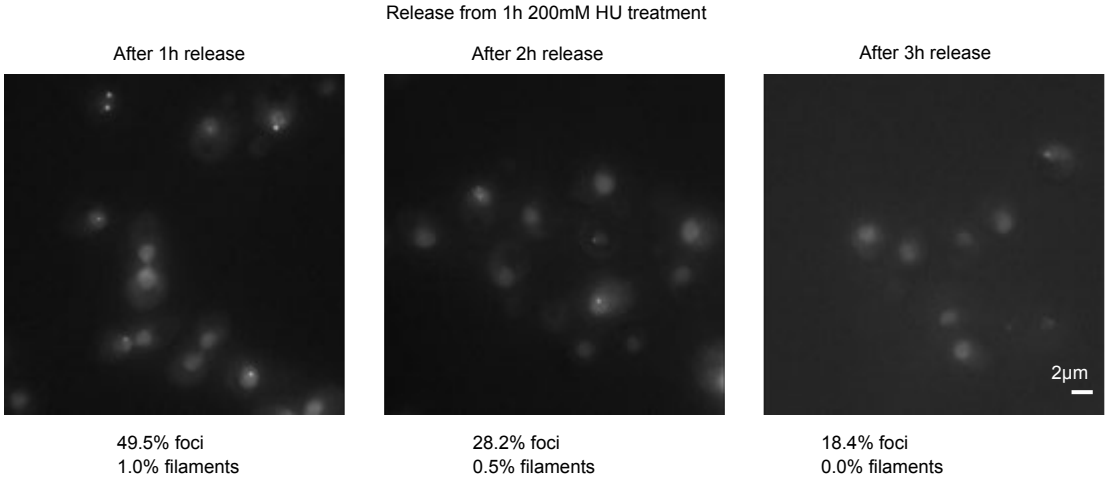
Release from 1h 200mM HU treatment
After 1h release
After 2h release
After 3h release
2µm
49.5% foci
1.0% filaments
28.2% foci
0.5% filaments
18.4% foci
0.0% filaments

B

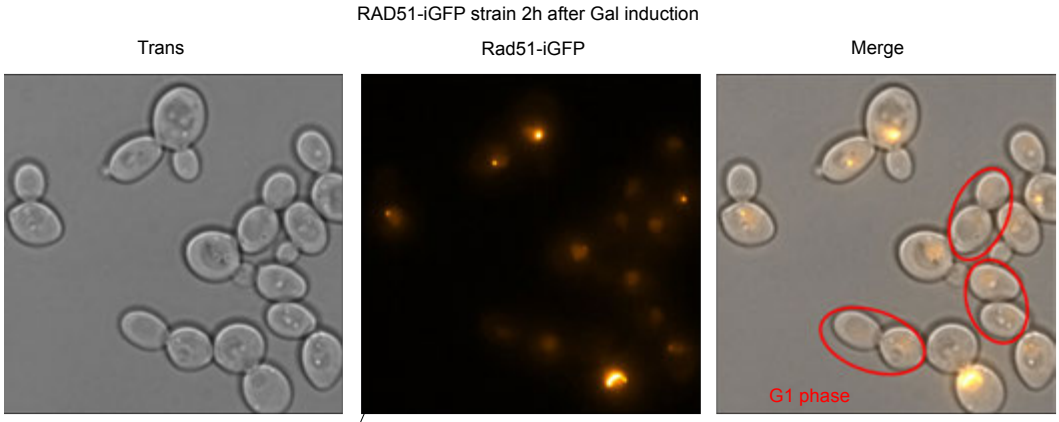
RAD51-iGFP strain 2h after Gal induction
Trans
Rad51-iGFP
Merge
G1 phase

C

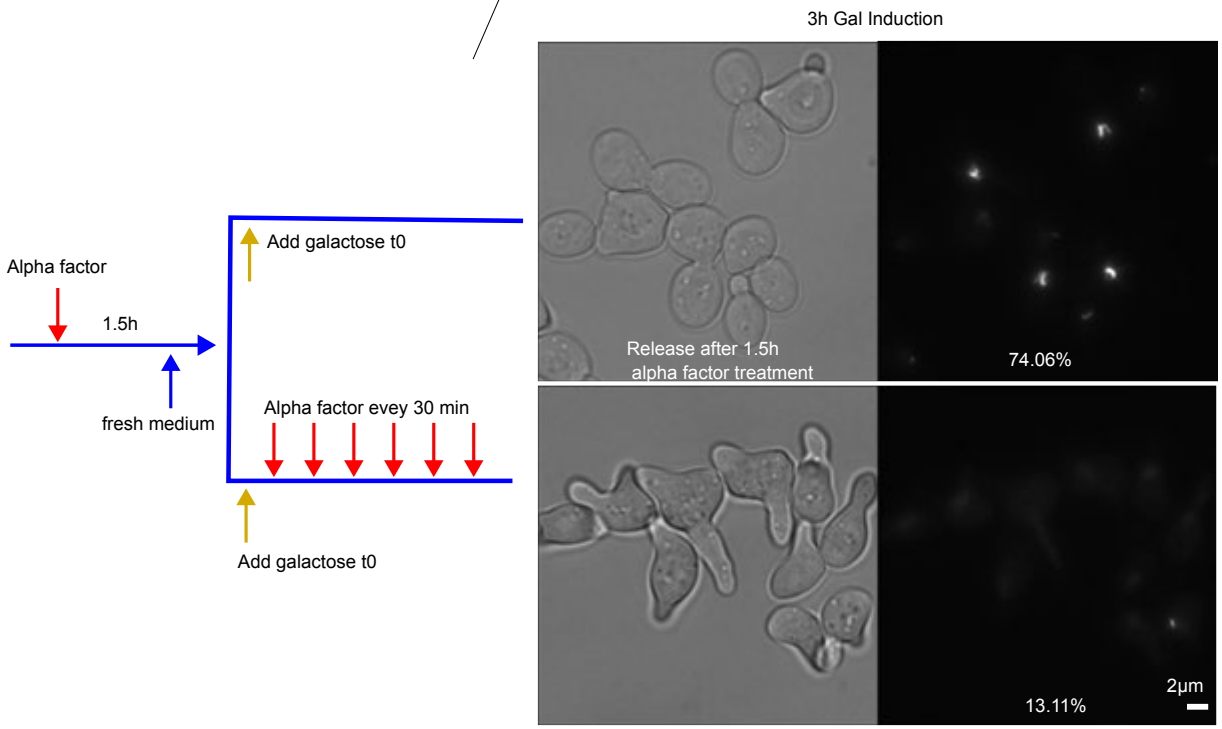
3h Gal Induction
Alpha factor
1.5h
fresh medium
Add galactose t0
Alpha factor evey 30 min
Add galactose t0
Release after 1.5h
alpha factor treatment
74.06%
13.11%
2µm

Extended Data Figure 5: Effects of Sgs1 and Exo1 on Rad51 filament intensities and distribution of filament length in diploid and haploid cells.

A. Comparison of total intensities of Rad51 filaments in WT, *sgs1*Δ, *exo1*Δ, *sgs1*Δ *exo1*Δ strains as indicated (n=608 Rad51 filaments are analyzed, two-sided Wilcoxon rank sum test, **** represents $p<0.0001$). On each box, the central mark indicates the median, and the bottom and top edges of the box indicate the 25th and 75th percentiles, respectively. The whiskers extend to the most extreme data points not considered outliers, and the outliers are plotted individually using the '+' marker symbol. **B.** Distributions of filament length in haploid (left) and diploid (right) strains, same data as in Figure 2C. n=1720 filaments are analyzed from 2 independent experiments.

A

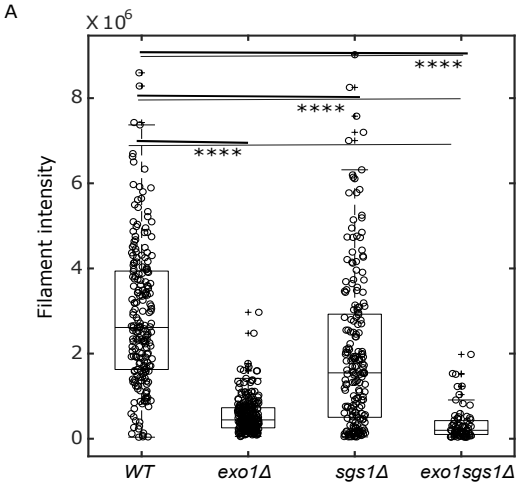
X 10^6
Filament intensity
8
6
4
2
0
****
****
****
WT
exo1Δ
sgs1Δ
exo1sgs1Δ

B

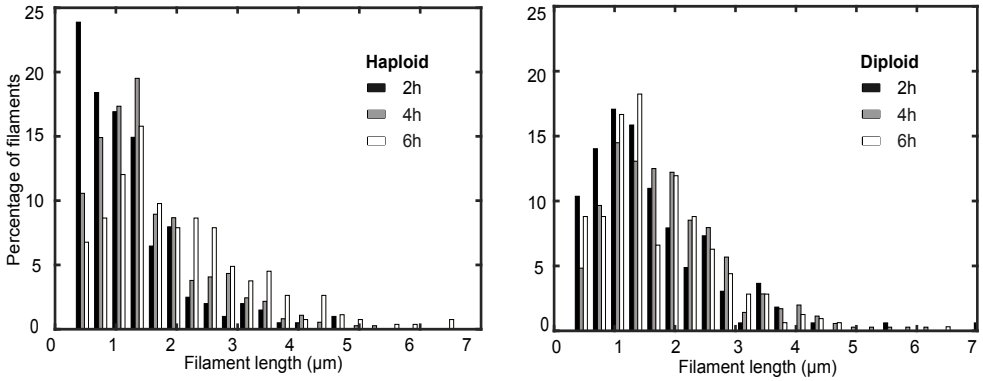
Percentage of filaments
25
20
15
10
5
0
Haploid
2h
4h
6h
0 1 2 3 4 5 6 7
Filament length (μm)
Diploid
2h
4h
6h
Filament length (μm)

Extended Data Figure 6: Effects of Rad54 on Rad51 structures.

A. Representative images (Transmitted-light image and GFP channel fluorescent image) of Rad51-iGFP strains in WT and mutants 4 hours after DSB induction as indicated. B. Percentages of foci, globular structures, and filaments in (n>100 cells examined per experiment, per condition with a total of n=3485 cells examined over 2 experiments) on the same strains as in A.

A

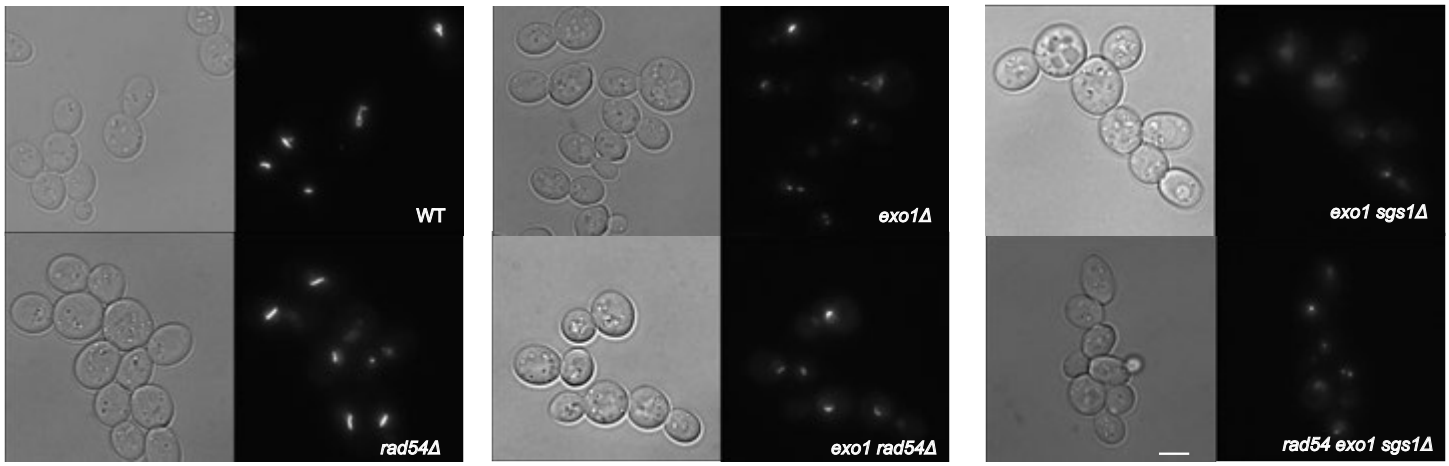
Rad51-iGFP 4h after DSB induction
WT
exo1Δ
exo1 sgs1Δ
rad54Δ
exo1 rad54Δ
rad54 exo1 sgs1Δ

B

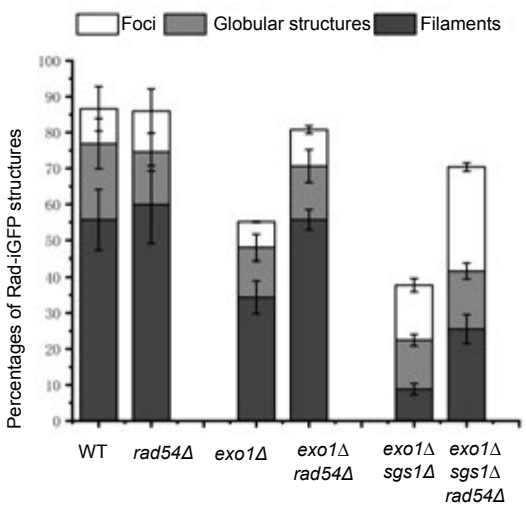
Foci
Globular structures
Filaments
Percentages of Rad-iGFP structures
100
90
80
70
60
50
40
30
20
10
0
WT
rad54Δ
exo1Δ
exo1Δ rad54Δ
exo1Δ sgs1Δ
exo1Δ sgs1Δ rad54Δ

Extended Data Figure 7: Variety of nuclear Rad51 filament shapes observed in haploid and diploid living cells expressing Rad51-iGFP and by immuno-fluorescence in cells expressing the untagged Rad51 protein.

A. Representative fluorescence images a Rad51-iGFP Nup-mCherry strain at 2, 4, 6 hours after DSB induction. GFP channel and RFP channel are combined, Z-projection is applied on fluorescent images**.** Representative filaments of WT haploid and diploid strains at different time after galactose induction. **C.** Untagged Rad51 localized by Immunofluorescence 6 hours after DSB induction show the same classes of filament shapes observed in cells expressing the untagged Rad51 protein.

A

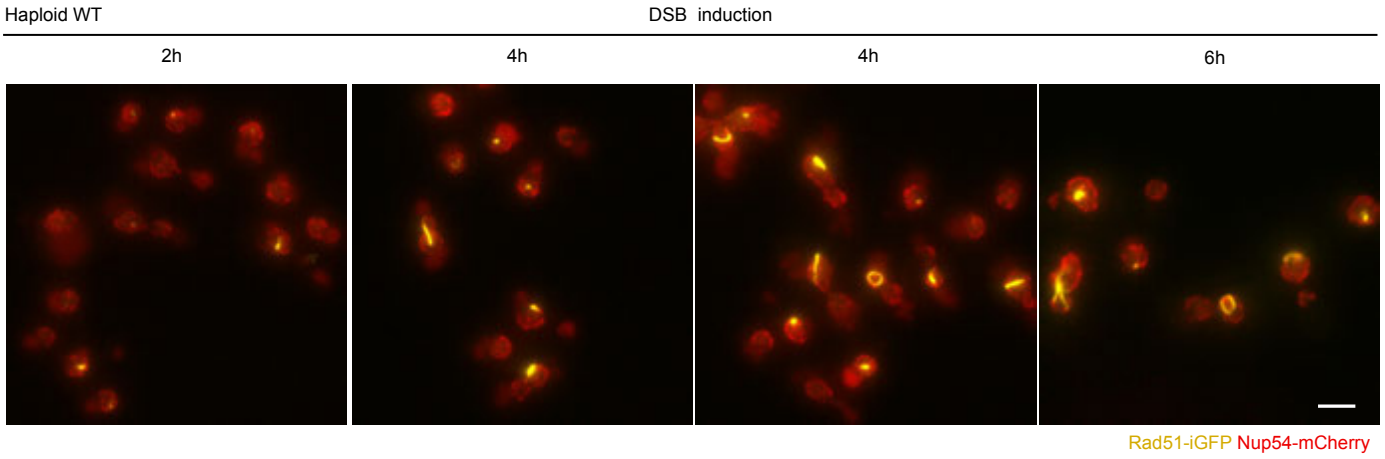
Haploid WT
DSB induction
2h
4h
4h
6h
Rad51-iGFP Nup54-mCherry

B

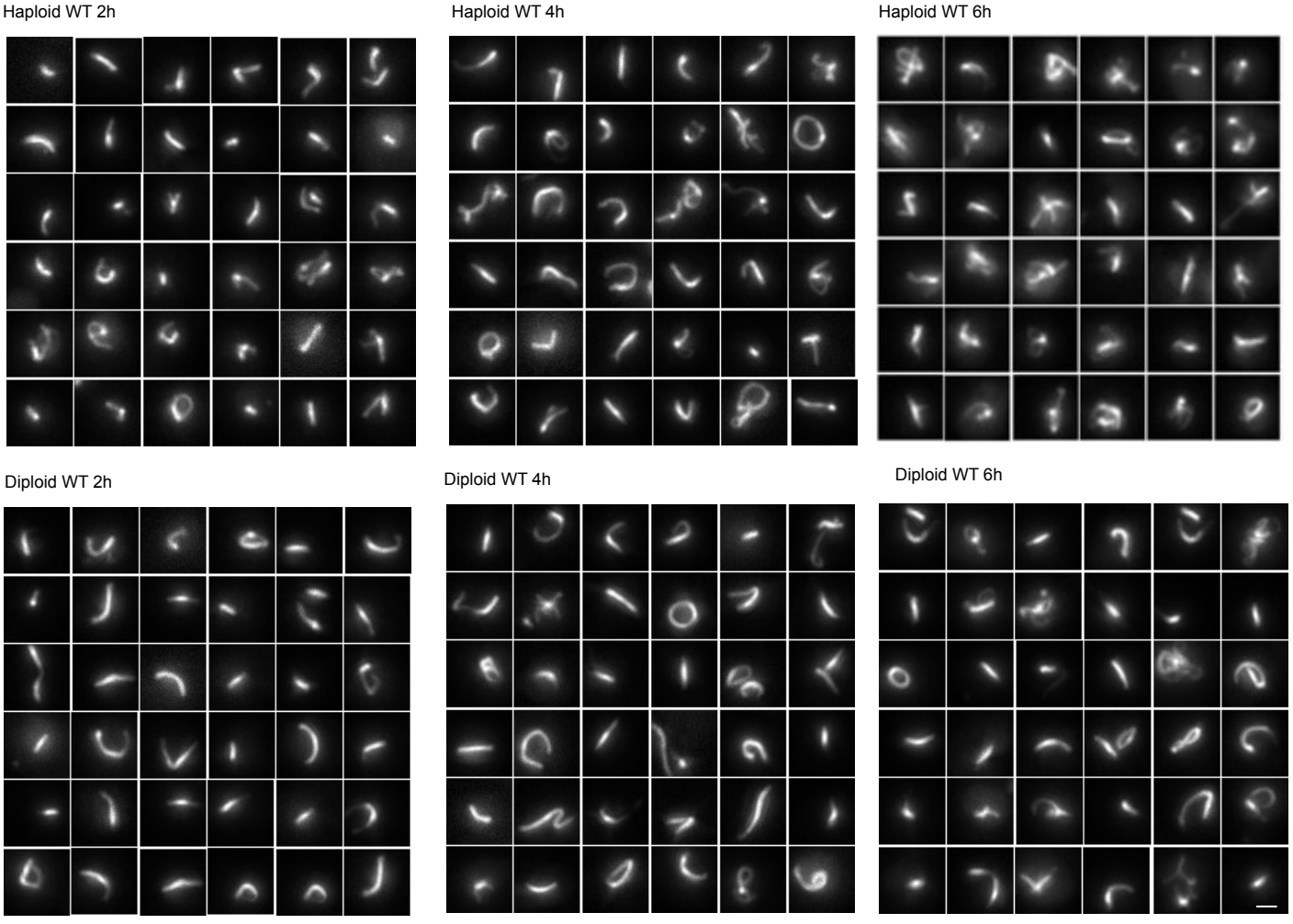
Haploid WT 2h
Haploid WT 4h
Haploid WT 6h
Diploid WT 2h
Diploid WT 4h
Diploid WT 6h

C

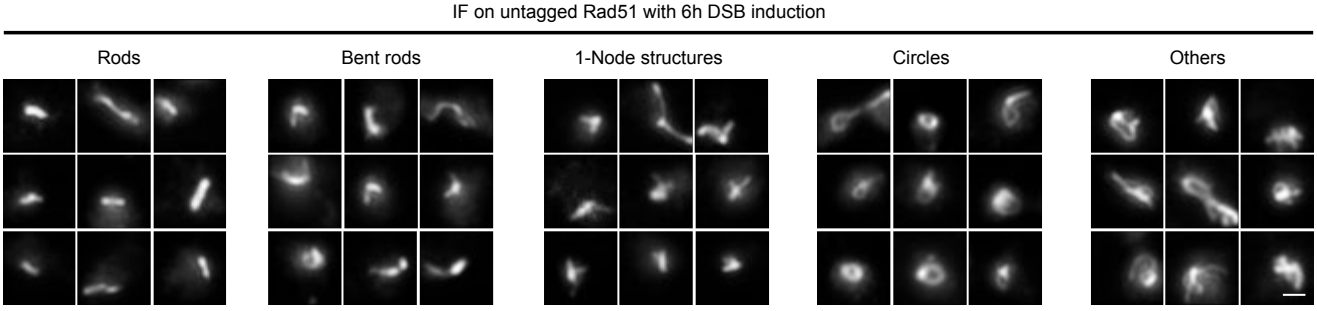
IF on untagged Rad51 with 6h DSB induction
Rods
Bent rods
1-Node structures
Circles
Others

Extended Data Figure 8: Rad51 filaments in mutants

A. Representative filaments of WT and mutants at 6h after galactose induction, Z-projection is applied. **B.** Distributions of class1 and class2 filament length (Rods and bent rods) in WT and srs2Δ 2,4 or 6 h after galactose induction, statistical test: two-side Wilcoxon rank sum test, 2 h, p=0.1187;4h p=0.0409;6h p=0.0025. n=540 Rad51 filaments analyzed from 2 experiments. On each box, the central mark indicates the median, and the bottom and top edges of the box indicate the 25th and 75th percentiles, respectively. The whiskers extend to the most extreme data points not considered outliers, and the outliers are plotted individually using the '+' marker symbol. Scale bars: 2 μm.

A

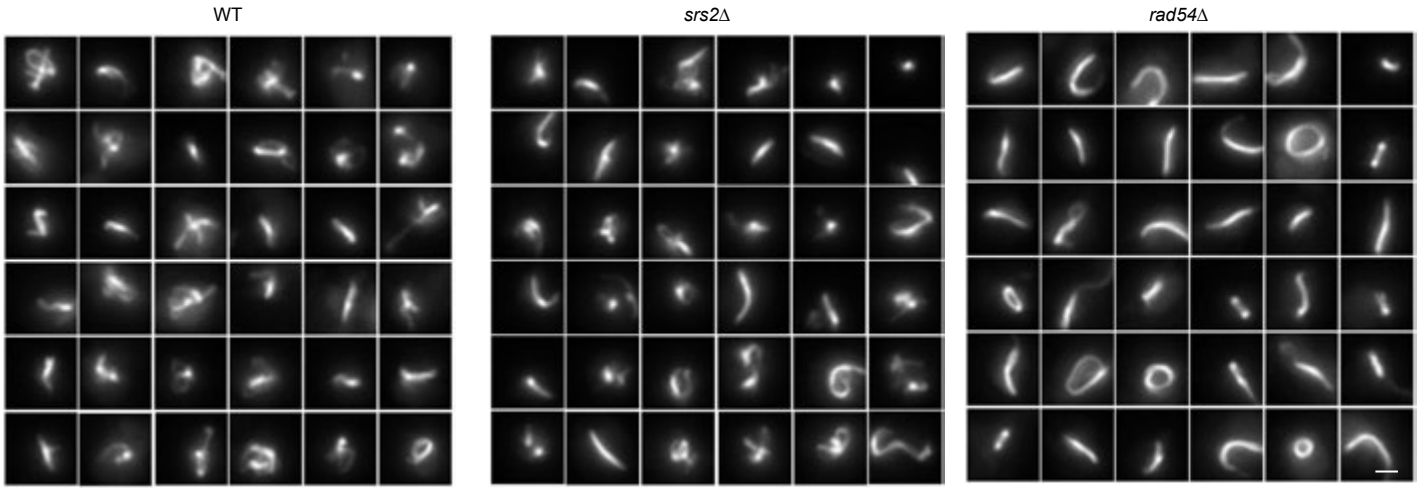
Rad51 filaments after 6h DSB induction
WT
srs2Δ
rad54Δ

B

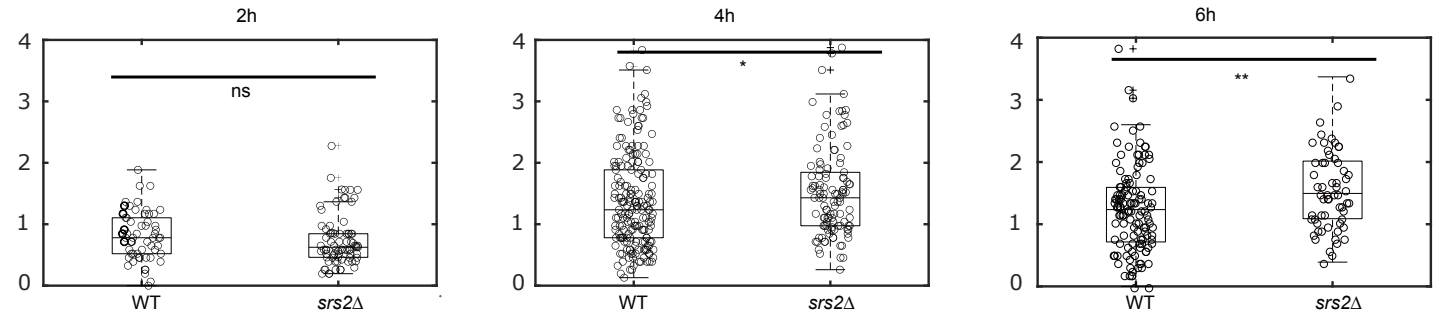
Rad51 filament length (µm) class 1 and 2
2h
4h
6h
ns
*
**
0
1
2
3
4
WT
srs2Δ

Extended Data Figure 9: Dynamics of Rad51 filaments in *srs2*Δ or *rad54*Δ haploid and wildtype diploid cells.

A. Examples of time-lapse images in WT and mutants upon DSB, images acquired every 2 minutes, Z-projection is applied. **B.** Number of frames from Rad51 foci to filaments (>6 pixel) in WT and mutants upon DSB (n=41 movies from 4 experiments). On each box, the central mark indicates the median, and the bottom and top edges of the box indicate the 25th and 75th percentiles, respectively. The whiskers extend to the most extreme data points not considered outliers, and the outliers are plotted individually using the '+' marker symbol. **C-D.** Examples of time-lapse images in Rad51-iGFP diploid strain upon DSB, images acquired every 2 minutes, Z-projection is applied (Movie S4-5).

Scale bar: 2µm

A

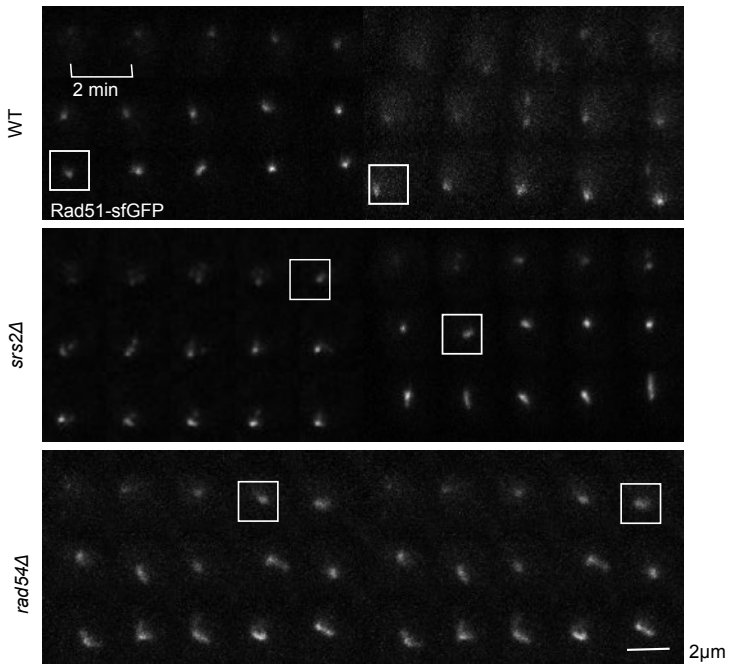

B

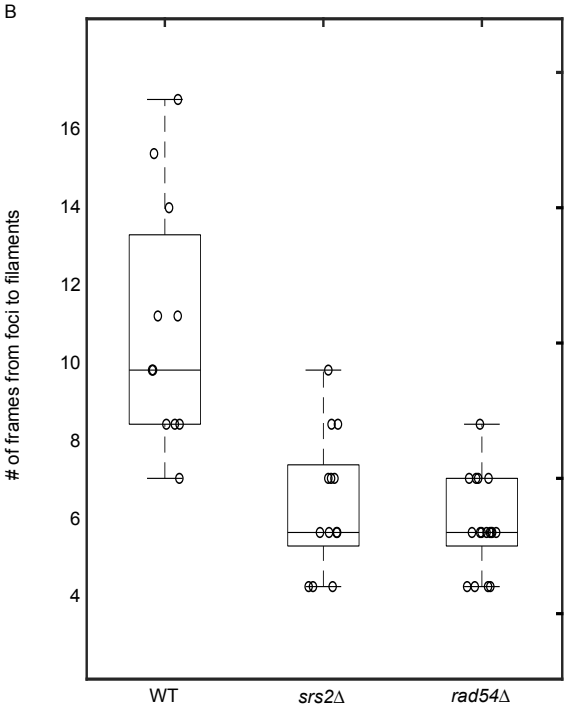

C Rad51-iGFP diploid after 70min Gal induction

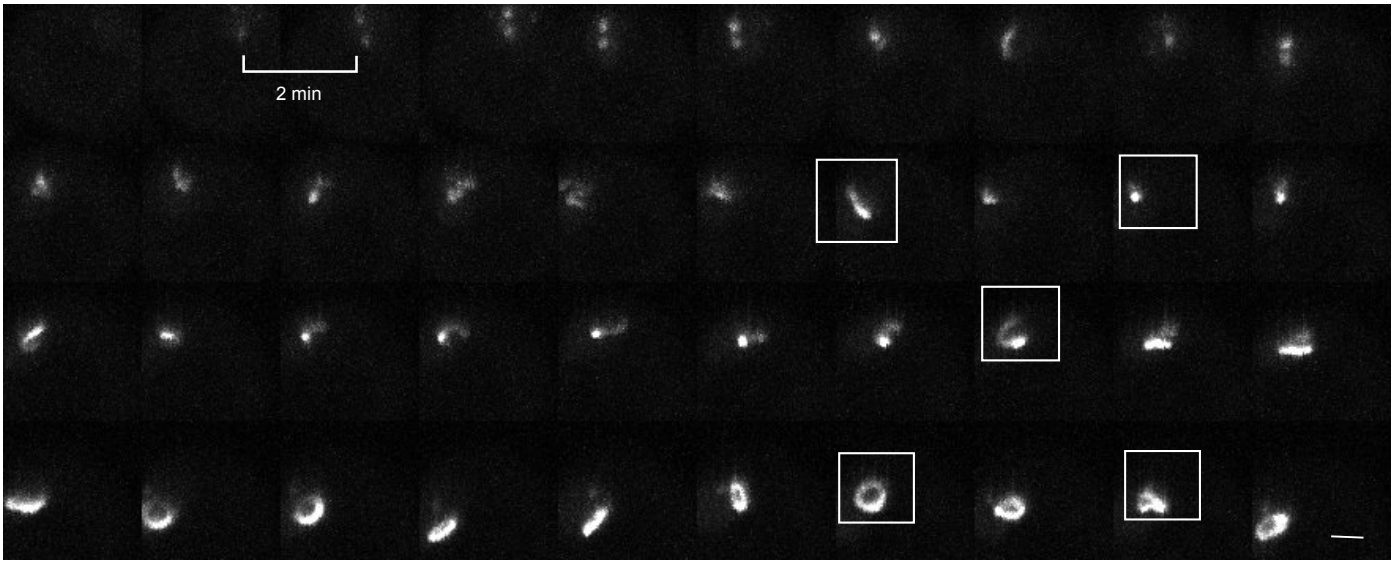

D Rad51-iGFP diploid after 225min Gal induction

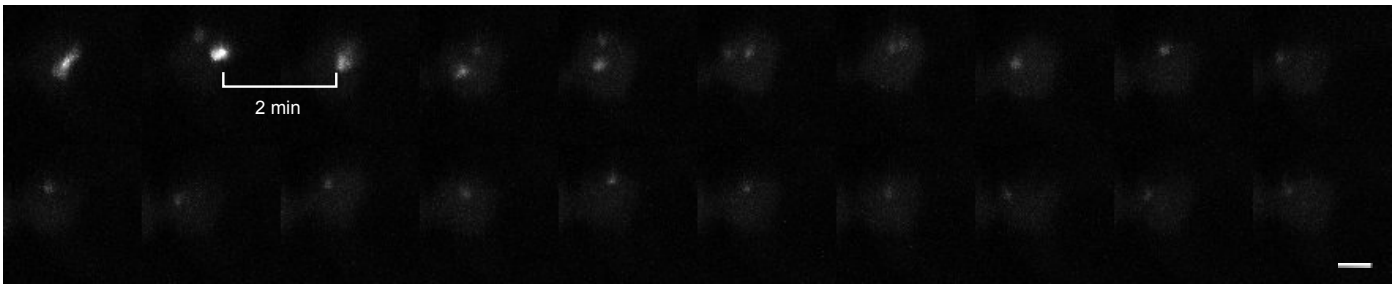

Extended Data Figure 10: The ATPase dead mutant Rad51-K191 does not form filament in living cells; Srs2 or Rad54 are not required for compaction/extension events.

A. Representative images (Transmitted-light image and GFP channel fluorescent image) and average percentages of foci, globular structures, and filaments in Rad51-iGFP and Rad51-K191R-iGFP strain 4 hours after DSB induction. Z-projection is applied. Of note, gray levels are set between 100 and 4500 before 16 to 8-bit conversion to visualize wild-type Rad51 structures and to 100-1500 to visualize Rad51-K191R structures (n=1186 cells in 2 experiments, data are presented as mean values +/- SEM). **B-C.** Examples of time-lapse images in Rad51-iGFP mutant strains upon DSB, images acquired every 2 minutes, Z-projection is applied (Movie S6-7). Red rectangle: Compacted Rad51 structures. Scale bars: 2 µm.

A

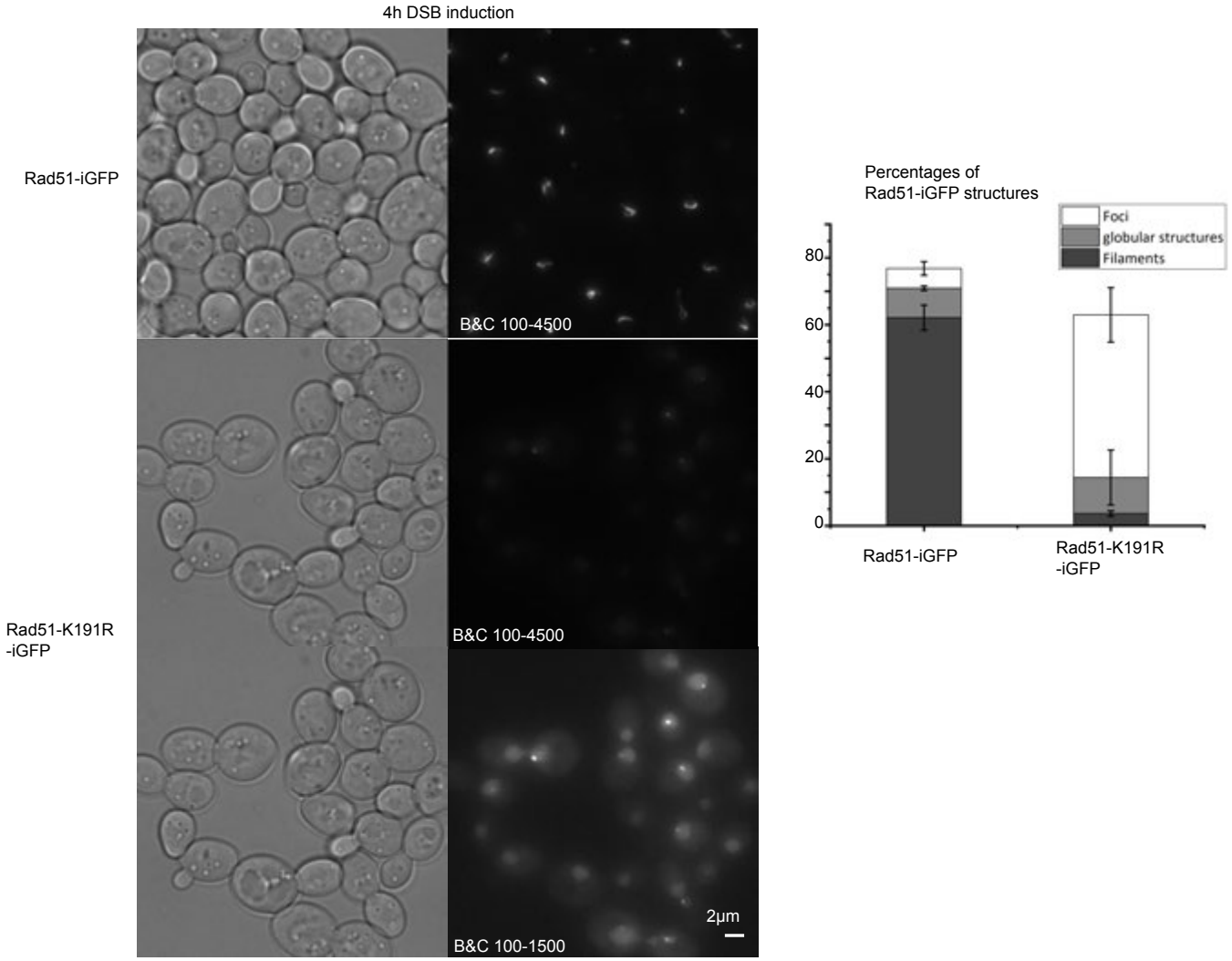

B

Rad51-iGFP *srs2* Δ after 70min Gal induction

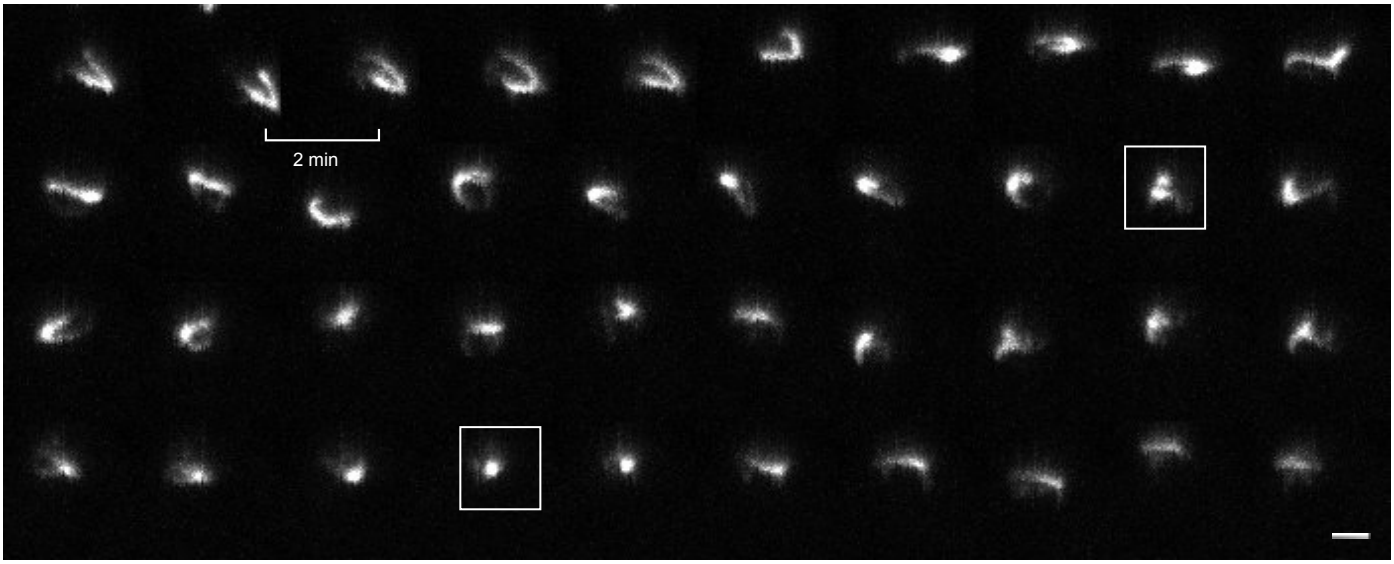

C

Rad51-iGFP *rad54*Δ after 190 min Gal induction

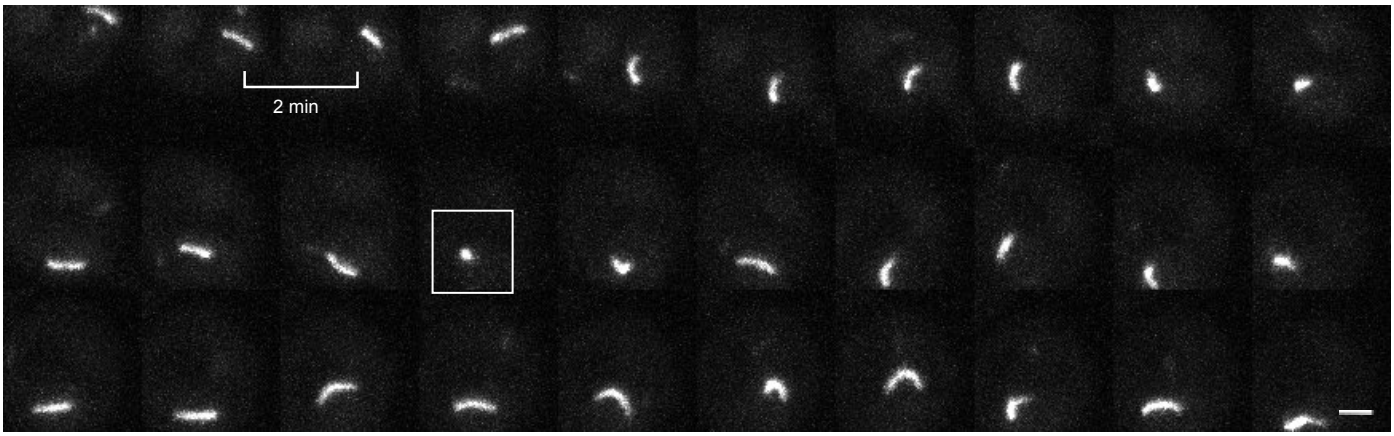

Supplementary Information

Tables S1 to S4

Movies S1 to S7

Table S1. List of strains used in the study

Strain name	Genotype
yAT3392	*MATa ADE2 RAD5+ lys2::ura3-ISceIcutsite(loxP) trp1::Galp-I-SceI-TRP1 ura3Δ::KanMX*
yAT3799	*MATa ADE2 RAD5+ lys2::ura3-ISceIcutsite(loxP) trp1::Galp-I-SceI-TRP1 ura3Δ::KanMX rad51Δ::hph*
W4121-20D	*MATa ADE2 bar1::LEU2 trp1-1 LYS2 RAD5 YFP-RAD51*
yAT3515	*MATa ADE2 RAD5+ lys2::ura3-ISceIcutsite(loxP) trp1::Galp-I-SceI-TRP1 ura3Δ::KanMX RAD51-iGFP1*
yAT3880	*MATa ADE2 RAD5+ lys2::ura3-ISceIcutsite(loxP) trp1::Galp-I-SceI-TRP1 ura3Δ::KanMX RAD51-iGFP2*
yAT3390	*MATa ADE2 RAD5+ lys2::ura3-ISceIcutsite(loxP) trp1::Galp-I-SceI-TRP1*
yAT4041	*MATa ADE2 RAD5+ lys2::ura3-ISceIcutsite(loxP) trp1::Galp-I-SceI-TRP1 Rad51-iGFP2*
yAT3971	*MATa/αADE2/ADE2 RAD5/RAD5 LSY2/lys2::ura3-ISceIcutsite(loxP) TRP1/trp1::Galp-ISCeI-TRP1 URA3/ura3Δ::KanMX RAD51-iGFP2/RAD51-iGFP2*
yAT4284	*MATa/αADE/ADE2 ARS607/ARS607::TRP1::Lacop::LexA ura3::CloNat/ ura3Δ::KanMX RAD5+/rad5 lys2::ura3-ISceIcutsite(loxP) /lys2) trp1::Galp-I-SceI-TRP1 RAD51-iGFP2/RAD51 his3::ADHp-LacIsp-mCherry(HIS) /his3*
yAT4206	*ADE2/ADE2 RAD5+/RAD5+ lys2::ura3-ISceIcutsite(loxP)/ lys2:: LacO (TRP1) trp1::Galp-I-SceI-TRP1/trp1 his/his::LacI mCherry(His) ura3Δ::KanMX/ura3::CloNAT RAD51-iGFP2/RAD51*
yAT3976	*MATa ADE2 RAD5+ lys2::ura3-ISceIcutsite(loxP) trp1::Galp-I-SceI-TRP1 ura3Δ::KanMX RAD51-iGFP2 exo1::hph*
yAT4034	*MATa ADE2 RAD5+ lys2::ura3-ISceIcutsite(loxP) trp1::Galp-I-SceI-TRP1 ura3Δ::KanMX RAD51-iGFP2 sgs1::CloNAT*
yAT4024	*MATa ADE2 RAD5+ lys2::ura3-ISceIcutsite(loxP) trp1::Galp-I-SceI-TRP1 ura3Δ::KanMX RAD51-iGFP2 exo1::hph sgs1::CloNAT*
yAT4032	*MATa ADE2 RAD5+ lys2::ura3-ISceIcutsite(loxP) trp1::Galp-I-SceI-TRP1 ura3Δ::KanMX RAD51-iGFP2 rad52::CloNAT*
yAT3974	*MATa ADE2 RAD5+ lys2::ura3-ISceIcutsite(loxP) trp1::Galp-I-SceI-TRP1 ura3Δ::KanMX RAD51-iGFP2 srs2Δ::HIS*
yAT4023	*MATa ADE2 RAD5+ lys2::ura3-ISceIcutsite(loxP) trp1::Galp-I-SceI-TRP1 ura3Δ::KanMX RAD51-iGFP2 rad54::CloNAT*
yAT4354	*MATa ADE2 RAD5+ lys2::ura3-ISceIcutsite(loxP) trp1::Galp-I-SceI-TRP1 ura3Δ::KanMX Rad51-GFP(HPH)*
yAT4256	*MATa ADE2 RAD5+ lys2::ura3-ISceIcutsite(loxP) trp1::Galp-I-SceI-TRP1 ura3Δ::KanMX RAD51-iGFP2 exo1::hph sgs1::CloNAT. rad54::CloNAT*
yAT3690	*MATa ADE2 RAD5+ lys2::ura3-ISceIcutsite(loxP) trp1::Galp-ISceI-TRP1 ura3Δ::KanMX RAD51-iGFP1 Nup57::NUP57-mCherry(HpH)*
yAT2604	*MATa ade2-1::ADE2 DDC1-CFP SPC42::SPC42-mcherry(KanMX) SPC110-YFP::HIS3*
yAT4502	*MATaADE2 RAD5+ lys2::ura3-ISceIcutsite(loxP) trp1::Galp-ISCeI-TRP1 ura3Δ::KanMX RAD51-iGFP2 rad54::CloNAT exo1::HPH*
yAT4552	*MATa ADE2 RAD5+ chrII: lys2::ura3-ISceIcutsite(loxP) chrII:490,700(URA3) ura3Δ::KanMX Rad51-iGFP2 trp1::Galp-ISCeI-TRP1*
yAT4553	*MATα ADE2 RAD5 MET15 RAD51-iGFP2 + pCEN-Galp-HO-TRP1*

Table S2. List of primers used in this study

Primers for plasmid construction	
	Sequence
Guide Rad51	am2449 ATCTGGCGGATTGCAGGAGCAAG am2450 AACCTTGCTCCTGCAATCCGCCA
dDNA Rad51-iGFP2	am558 CATTCCCTGAGCATTCCAAC am2401 CCTGAATTCACCGAAAAGCTCA
dDNA Rad51-iGFP1	am2334 GCAACGGTAGCAGCGAAGATATTGAGGCCACCAACGGCTCCGGCGA TGGTGGAGGTGCTGGATCTGCTGGTGGTGCAGGTGGATCTAAAGGT GAAGAATTATT am2335 AGGCAGCTTCATCGTATGCTTCATCCTCCATTTCACCTTGCGCTTCTG CTTGCTCCTGCAATCCGCCACCACCAGCACCACCAGCAGAACCAGCA CCACCTTTGTACAATTCATCCATAC
Primers for ChIP	
Name	Sequence
OGG1	F CAATGGTGTAGGCCCCAAAG R ACGATGCCATCCATGTGAAGT
-200bp	F AAGGAACGTGCTGCTACTC R ACATCCAATGAAGCACACAAG
-600bp	F CGTCAGGGCCAAGGATGA R AGTACCATAGGTGATACCTGCCTTTT
-800bp	F TGATTTACCATTGGGCACAATTT R AATTTCCGCGGCAAAGG
-1.4kb	F TCGCAAAAATGCCGACAAT R GCTTGTCAAATCTTGGGACCAT
-5kb	F GCTCTGGCAACAAGAAAGAC R ACCGATCAATTCAGGCAAAAC
-8kb	F CTTTTCCCAACCCTTGTACC R GTTCCATTCGTCCCAATCTC
-12kb	F TCGAAGAAGTTTTGGAAGCTC R TAGCAGCGGCATTAGCATC
-18kb	F TCATCAAGCTCAACAAGCTC R GAAAACCGGACCAGGAATAG

Table S3. Filament lengths and intensities

Filament Median lengths in haploid and diploid strain (N>180, μm), two-side wilcoxon rank sum test, no adjustments for multiple comparisons.

	2h	4h	6h	P 2h *vs* 4h	P 2h *vs* 6h	P 4h *vs* 6h
Haploid	0.91	1.30	1.69	1.08e-07 ***	2.70e-18 ***	7.92e-08 ***
Diploid	1.30	1.69	1.43	1.32e-04 ***	7.01e-02 ns	1.08e-02 *

Filament Median lengths in WT, *srs2Δ* and *rad54Δ* strain (N>230, μm), two-side wilcoxon rank sum test, no adjustments for multiple comparisons.

	WT	*srs2Δ*	*rad54Δ*	P (WT *vs srs2Δ*)	P (WT *vs rad54Δ*)	P (*srs2Δ vs rad54Δ*)
4h	1.36	1.45	1.56	6.92e-01 ns	5.35e-05 ***	5.23e-05 ***
6h	1.75	1.82	2.40	8.41e-01 ns	3.60e-11 ***	1.97e-09 ***

Filament Median intensities in WT, *srs2Δ* and *rad54Δ* strain (N>230, a.u), two-side wilcoxon rank sum test, no adjustments for multiple comparisons.

	WT	*srs2Δ*	*rad54Δ*	P (WT *vs srs2Δ*)	P (WT *vs rad54Δ*)	P (*srs2Δ vs rad54Δ*)
4h	1210	1400	1280	5.88e-16 ***	35.61e-03 ***	3.02e-06 ***

Table S4. Search time, parameters used, theoretical estimates and results of simulations

Parameters	Two compact loci	Stable filament	Dynamic filament
A (um2/sec)	0.01	0.01	0.01
Nuclear radius, R (um)	1.4	1.4	1.4
Filament length, L (um)	-	1.2	1.2
tau and tau0 (sec)	-	-	1000,100
Theory search time (h)	10.7	4.9	1.8
Simulations: Median search time with 95% CI (h)for 50nm cutoff	9.0 (7.4 10.9)	4.7 (4.1 5.1)	2.2 (2.0 2.3)
% finished in 8	46%	66%	92%

		Search time in (h)				
	Rcut(nm)	Mean	Median (95% confidence)	%finished in simul.	%finished in 8h	Mean/ median
no-filament	25	31.3	29.5 (26.1;4.8)			
		0.73	0.17 1.06			
static filament	25	7.0	6.0 (5.5;6.6)	0.76	0.58	1.16
dynamic filament	25	3.9	3.1 (2.9;3.3)	1.00	0.88	1.28
no-filament	50	12.9	9.0 (.4;10.9)	0.97	0.46	1.44
static filament	50	6.1	4.7 (4.1;5.1)	0.81	0.66	1.30
dynamic filament	50	3.1	2.2 (2.0;2.3)	1.00	0.92	1.42
no-filament	100	5.9	4.5 (3.5;5.8)	0.84	0.69	1.31
static filament	100	5.2	3.8 (3.3;4.2)	0.88	0.72	1.38
dynamic filament	100	2.2	1.5 (1.4;1.6)	1.00	0.97	1.44

Movie S1: corresponding to Figure 4A. WT haploid cell imaged every 5 min, 90 min after galactose addition (I-SceI induction) showing the formation of a Rad51 filament. Z-projection is applied.

Movie S2: corresponding to Figure 4B. WT haploid cell imaged every 5 min, 150 min after galactose addition (I-SceI induction) showing the dynamic of a mature Rad51 filament adopting different shapes over time. Z-projection is applied.

Movie S3: corresponding to Figure 4C. WT haploid cell imaged every 2 mins, 70 min after galactose addition showing Rad51 filament undergoing compaction and extension events. Z-projection is applied.

Movie S4: corresponding to Extended Figure 9C. WT diploid cell imaged every 2 minutes, 70 min after galactose addition (I-SceI induction), showing the formation and dynamics of a Rad51 filament, undergoing compaction/retraction events, and adopting various shapes. Z-projection is applied.

Movie S5: corresponding to Extended Figure 9D. WT diploid cell imaged every 2 minutes, 225 min after galactose addition (I-SceI induction), showing the disassembly of the Rad51 filament.

Movie S6: corresponding to Extended Figure 10B. Haploid *srs2*Δ cell imaged every 2 minutes, 70 min after galactose addition (I-SceI induction), showing the dynamics of a Rad51 filament, undergoing compaction/retraction events, and adopting various shapes. Z-projection is applied.

Movie S7: corresponding to Extended Figure 10C. Haploid *rad54*Δ cell imaged every 2 minutes, 190 min after galactose addition (I-SceI induction), showing the dynamics of a Rad51 filament, undergoing compaction/retraction events.